



**HAL**  
open science

## **MEK-SHP2 inhibition prevents tibial pseudarthrosis caused by NF1 loss in Schwann cells and skeletal stem/progenitor cells**

Simon Perrin, Sanela Protic, Vincent Bretegnier, Ingrid Laurendeau, Oriane Duchamp de Lageneste, Nicolas Panara, Odile Ruckebusch, Marine Luka, Cécile Masson, Théodora Maillard, et al.

### ► To cite this version:

Simon Perrin, Sanela Protic, Vincent Bretegnier, Ingrid Laurendeau, Oriane Duchamp de Lageneste, et al.. MEK-SHP2 inhibition prevents tibial pseudarthrosis caused by NF1 loss in Schwann cells and skeletal stem/progenitor cells. *Science Translational Medicine*, 2024, 16 (753), pp.eadj1597. 10.1126/scitranslmed.adj1597 . hal-04646302

**HAL Id: hal-04646302**

**<https://hal.u-pec.fr/hal-04646302v1>**

Submitted on 12 Jul 2024

**HAL** is a multi-disciplinary open access archive for the deposit and dissemination of scientific research documents, whether they are published or not. The documents may come from teaching and research institutions in France or abroad, or from public or private research centers.

L'archive ouverte pluridisciplinaire **HAL**, est destinée au dépôt et à la diffusion de documents scientifiques de niveau recherche, publiés ou non, émanant des établissements d'enseignement et de recherche français ou étrangers, des laboratoires publics ou privés.

# **MEK-SHP2 inhibition prevents tibial pseudarthrosis caused by *NF1* loss in Schwann cells and skeletal stem/progenitor cells**

Simon Perrin<sup>1</sup>, Sanela Protic<sup>1</sup>, Vincent Bretegnier<sup>1</sup>, Ingrid Laurendeau<sup>2</sup>, Oriane Duchamp de Lageneste<sup>1</sup>, Nicolas Panara<sup>2</sup>, Odile Ruckebusch<sup>3</sup>, Marine Luka<sup>4,5</sup>, Cécile Masson<sup>6,7</sup>, Théodora Maillard<sup>8</sup>, Fanny Coulpier<sup>1</sup>, Stéphanie Pannier<sup>9</sup>, Philippe Wicart<sup>9</sup>, Smail Hadj-Rabia<sup>10</sup>, Katarzyna J. Radomska<sup>1</sup>, Mohammed Zarhrate<sup>7,11</sup>, Mickael Ménager<sup>4,5</sup>, Dominique Vidaud<sup>2,8</sup>, Piotr Topilko<sup>1</sup>, Béatrice Parfait<sup>2,8</sup>, and Céline Colnot<sup>1,\*</sup>

<sup>1</sup> Univ Paris Est Creteil, INSERM, IMRB, 94000, Creteil, France

<sup>2</sup> INSERM UMR S1016, Institut Cochin, Université Paris Cité, 75014, Paris, France

<sup>3</sup> Univ Paris Est Creteil, INSERM, IMRB, Plateforme de Cytométrie en flux, 94000, Creteil, France

<sup>4</sup> Paris Cité University, Imagine Institute, Laboratory of Inflammatory Responses and Transcriptomic Networks in Diseases, Atip-Avenir Team, INSERM UMR 1163, 75015, Paris, France.

<sup>5</sup> Labtech Single-Cell@Imagine, Imagine Institute, INSERM UMR 1163, 75015, Paris, France.

<sup>6</sup> Bioinformatics Core Facility, Institut Imagine-Structure Fédérative de Recherche Necker, INSERM U1163, 75015, Paris, France.

<sup>7</sup> INSERM US24/CNRS UAR3633, Paris Cité University, 75015, Paris, France

<sup>8</sup> Service de Médecine Génomique des Maladies de Système et d'Organe, Hôpital Cochin, DMU BioPhyGen, Assistance Publique-Hôpitaux de Paris, AP-HP, Centre-Université Paris Cité, F-75014 Paris, France

<sup>9</sup> Department of Pediatric Orthopedic Surgery and Traumatology, Necker-Enfants Malades Hospital, AP-HP, Paris Cité University, 75015, Paris, France

<sup>10</sup> Department of Dermatology, Reference Center for Rare Skin Diseases (MAGEC), Imagine Institute, Necker-Enfants Malades Hospital, AP-HP, Paris Cité University, 75015, Paris, France.

<sup>11</sup> Genomics Core Facility, Institut Imagine-Structure Fédérative de Recherche Necker, INSERM U1163, 75015, Paris, France.

\*Corresponding author: [celine.colnot@inserm.fr](mailto:celine.colnot@inserm.fr)

29 **One Sentence Summary**

30

31 Combined MEK-SHP2 inhibition prevents fibrotic failure to heal in a preclinical model of congenital  
32 pseudarthrosis of the tibia.

33 **Abstract**

34 Congenital pseudarthrosis of the tibia (CPT) is a severe pathology marked by spontaneous bone  
35 fractures that fail to heal leading to fibrous nonunion. Half of patients with CPT are affected by the  
36 multisystemic genetic disorder neurofibromatosis type 1 (NF1), caused by mutations in the *NF1* tumor  
37 suppressor gene, a negative regulator of RAS-MAPK signaling pathway. Here, we analyzed patients  
38 with CPT and *Prss56-Nf1* knockout mice to elucidate the pathogenic mechanisms of CPT-related fibrous  
39 nonunion and explored a pharmacological approach to treat CPT. We identified *NF1*-deficient Schwann  
40 cells and skeletal stem/progenitor cells (SSPCs) in pathological periosteum as affected cell types driving  
41 fibrosis. Whereas *NF1*-deficient SSPCs adopted a fibrotic fate, *NF1*-deficient Schwann cells produced  
42 critical paracrine factors including TGF $\beta$  and induced fibrotic differentiation of wild-type SSPCs. To  
43 target both *NF1*-deficient Schwann cells and SSPCs, we used combined MEK and SHP2 inhibitors to  
44 counteract the elevated RAS-MAPK signaling in human SSPCs. Combined MEK-SHP2 inhibition in vivo  
45 prevented fibrous nonunion in the *Prss56-Nf1* knockout mouse model, providing a promising therapeutic  
46 strategy for the treatment of fibrous nonunion in CPT.

47

## 48 **Introduction**

49

50 Congenital pseudarthrosis of the tibia (CPT) is a rare but severe pathology that manifests mostly in  
51 children prior to 2 years of age. Patients with CPT present with tibial bowing at birth leading to  
52 spontaneous fracture and failure to heal due to fibrous nonunion. CPT treatment is exclusively surgical  
53 and remains highly challenging, with substantial risk of re-fracture or amputation (1, 2). Pharmacological  
54 treatments are needed to improve CPT management, but the pathogenic mechanisms remain poorly  
55 understood and a relevant pre-clinical model for CPT is lacking. CPT can be classified as isolated CPT  
56 of unknown etiology, or NF1-related CPT in patients diagnosed with neurofibromatosis type 1 (NF1).  
57 NF1 is one of the most common multisystemic genetic disorders that affects 1 in 3000 individuals.  
58 Patients with NF1 can exhibit a variety of symptoms, including benign nerve sheath tumors, called  
59 cutaneous and plexiform neurofibromas (NFBs), skin hyperpigmentation (Café-au-lait macules,  
60 CALMs), learning disabilities, and bone manifestations (3). NF1 is caused by heterozygous mutations  
61 in the *NF1* gene encoding the tumor-suppressor neurofibromin, a negative regulator of RAS and the  
62 MAPK pathway. The diverse NF1 symptoms result from a second somatic mutational event in specific  
63 tissues and cell types. NFBs and CALMs have been shown to result from *NF1* biallelic inactivation in  
64 Schwann cells and melanocytes respectively (4–8).

65

66 Although *NF1* biallelic inactivation has been reported in CPT, the specific cell types harboring *NF1* loss  
67 have not been identified. The presence of pathological periosteum suggests the involvement of the  
68 periosteum in the pathogenesis of CPT (9–11). Located on the outer layer of bones, the periosteum is  
69 essential for bone regeneration and contains a major source of skeletal stem/progenitor cells (SSPCs)  
70 as well as immune, endothelial, and neural cells (12–18). Until now, investigations of NF1 bone  
71 manifestations in mouse models have focused mainly on the skeletal lineage and the consequences of  
72 *Nf1* gene inactivation on fracture repair have been examined using bone-specific Cre lines (19–23).  
73 However, targeting *Nf1* solely in bone lineages does not recapitulate other NF1 features. Recent work  
74 by Radomska et al. reported the *Prss56-Nf1* knockout (KO) mouse model that faithfully recapitulates  
75 several NF1 symptoms, demonstrating that *Prss56*-expressing boundary cap (BC) cells are the cellular  
76 origin of cutaneous and plexiform NFBs, as well as skin hyperpigmentation (24). Located at the surface  
77 of the neural tube during development, BC cells are transient neural crest-derived populations giving  
78 rise to various derivatives in nerves and skin such as Schwann cells, fibroblasts, and melanocytes (25).

79 The common BC origin of NF1 dermatological and neurological lesions raises the question of a common  
80 cellular origin with NF1 bone manifestations.

81

82 Pharmacological interventions for NF1-related conditions are mostly targeting the RAS-MAPK signaling  
83 pathway. Several preclinical studies demonstrated the efficacy of MEK-inhibitors to counteract the  
84 elevated RAS-MAPK signaling due to reduced neurofibromin activity in cells lacking *NF1* (26, 27). This  
85 led to a successful clinical trial and Food and Drug Administration (FDA) approval of selumetinib in 2020  
86 for patients with inoperable plexiform NFBs (27–29). MEK inhibitors have also been tested in animal  
87 models exhibiting bone phenotypes associated with *Nf1* loss of function in bone cells but showed limited  
88 effects (19, 22). Other approaches such as BMP2, bisphosphonates, lovastatin, and beta-catenin  
89 inhibition have also shown variable results (19, 30–32).

90

91 This study aimed to identify the cellular origin and pathogenic mechanisms of CPT to develop efficient  
92 therapeutic strategies. Combined analyses of samples from patients with CPT and from the *Prss56-Nf1*  
93 KO mouse model unraveled the conserved mechanisms of CPT between mice and humans. We  
94 performed genetic analyses of patient pseudarthrosis tissues to search for *NF1* second hit mutations in  
95 various cell types in the periosteum including SSPCs and Schwann cells. To elucidate the role of RAS-  
96 MAPK pathway overactivation in CPT, we investigated the tibial pseudarthrosis phenotype of *Prss56-*  
97 *Nf1* KO mice that carry *Nf1* gene inactivation in BC derived SSPCs and Schwann cells in periosteum.  
98 Based on these results, we posited that combining MEK with SHP2 inhibition would drive robust  
99 responses in NF1 bone lesions, as SHP2 is a master positive regulator of RAS-MAPK pathway upstream  
100 of RAS (33, 34). We tested the efficacy of combined MEK and SHP2 inhibition to prevent pseudarthrosis  
101 in the pre-clinical *Prss56-Nf1* KO mouse model.

102

103

104

## 105 **Results**

### 106 **SSPCs and Schwann cells within pathological periosteum carry *NF1* biallelic inactivation in CPT**

107 To investigate the tissue specificity of *NF1* biallelic inactivation in CPT, we performed *NF1* targeted  
108 sequencing of tissues from the affected pseudarthrosis (PA) site, the unaffected iliac crest (IC), and  
109 blood of 17 patients undergoing surgical treatment (Figure 1A-B, Table S1). We detected *NF1* biallelic  
110 inactivation primarily in the periosteum of the PA site (13/17 patients, Figure 1C). We also identified *NF1*  
111 biallelic inactivation in fibrous tissue (6/17 patients), bone (6/17) and bone marrow (4/17) at the PA site  
112 and in skeletal muscle (3/14) and skin (2/14) adjacent to the PA site. *NF1* biallelic inactivation was not  
113 detected in blood or IC. Of note, 2 *NF1* hits were detected in patients with *NF1*-related CPT as well as  
114 patients with isolated CPT, revealing that most CPTs are caused by *NF1* loss of function (Figure 1D).  
115 We observed the same *NF1* second hit in tibia and fibula in 4/5 patients affected by combined tibia and  
116 fibula CPT (Figure S1A). Moreover, in 3 patients, we identified the same *NF1* second hit in PA  
117 periosteum, muscle and skin surrounding the PA site (Figure S1B). These results indicate that the  
118 second mutational event occurred during early skeletogenesis and was not restricted to the skeletal  
119 lineage. Next, we sought to identify the cell types carrying *NF1* biallelic inactivation in the periosteum.  
120 We detected 2 *NF1* hits in cultured periosteal SSPCs (pSSPCs) from 9 of the 13 patients carrying 2 hits  
121 in the periosteum (Figure 1E, Table S1). Thus, pSSPCs carry *NF1* biallelic inactivation but are not the  
122 only affected cell type. We then performed droplet digital PCR on sorted cell populations from PA  
123 periosteum of patient P15 (Figure S1C-G). The same *NF1* variants were detected in SSPCs and in  
124 Schwann cells, but not in endothelial or immune cells (Figure 1F, Figure S1E). This revealed that  
125 Schwann cells also carry *NF1* biallelic inactivation in CPT, and that mutated pSSPCs and Schwann cells  
126 in P15 are derived from a common lineage. *NF1* inactivation in periosteum led to an increased  
127 percentage of pERK+ cells in PA compared to IC periosteum (Figure 1G). Co-immunostaining of pERK  
128 and specific cell markers correlated with the genetic results as we observed the presence of increased  
129 percentage of pERK+CD90+ SSPCs and pERK+SOX10+ Schwann cells in PA periosteum compared  
130 to IC periosteum, but not of pERK+CD31+ endothelial cells, pERK+CD68+ immune cells, or  
131 pERK+ $\alpha$ SMA+ pericytes/smooth muscle cells (Figure 1H). The percentages of pERK+ SSPCs and  
132 Schwann cells at PA site were correlated, suggesting the presence of both mutated cell types in all  
133 patients (Fig. S1H). Overall, the results show that SSPCs and Schwann cells within periosteum are the  
134 cell types carrying *NF1* biallelic inactivation in CPT and that mutated pSSPCs and Schwann cells share  
135 a common origin.

136

137 ***Nf1* inactivation in BC-derived pSSPCs and Schwann cells cause tibial pseudarthrosis in mice**

138 To explore the role of SSPCs and SCs in CPT, we analyzed the *Prss56-Nf1* KO mouse model (24).  
139 Lineage tracing analyses in *Prss56<sup>Cre</sup>; R26<sup>tdTom</sup>* mice showed that BC-derived tdTom<sup>+</sup> cells are a rare  
140 cell population in adult bone found predominantly within the periosteum in uninjured tibia and correspond  
141 to Platelet-Derived Growth Factor Receptor  $\alpha$ <sup>+</sup> (PDGFR $\alpha$ <sup>+</sup>) SCA1<sup>+</sup> pSSPCs and SOX10<sup>+</sup> Schwann  
142 cells (Figure 2A, Figure S2-S3). Analyses from developmental stages to adulthood showed that *Prss56*  
143 expression was not detected in bone, indicating the BC-origin of tdTom<sup>+</sup> SSPCs and SCs in the  
144 periosteum of *Prss56<sup>Cre</sup>; R26<sup>tdTom</sup>* mice (Figure S4). To determine if *Prss56-Nf1* KO mice exhibit  
145 congenital pseudarthrosis, we analyzed their bone parameters and induced tibial fracture in 3-month-  
146 old *Prss56<sup>Cre</sup>; R26<sup>tdTom</sup>; Nf1<sup>fl/fl</sup>* (*Prss56-Nf1<sup>fl/fl</sup>*) and *Prss56<sup>Cre</sup>; R26<sup>tdTom</sup>; Nf1<sup>fl/-</sup>* (*Prss56-Nf1<sup>fl/-</sup>*) mutant mice,  
147 and *Prss56<sup>Cre</sup>; R26<sup>tdTom</sup>; Nf1<sup>+/+</sup>* (*Prss56-Nf1<sup>+/+</sup>*) controls. Although we only detected a mild reduction in  
148 tibial length of uninjured tibia (Figure S5), we observed a severe reduction in callus and bone volumes  
149 in both *Prss56-Nf1<sup>fl/fl</sup>* and *Prss56-Nf1<sup>fl/-</sup>* mutant mice through all stages of bone repair, as well as delayed  
150 cartilage formation and resorption (Figure S6A-B). From day 14 post-fracture, we observed persistence  
151 of fibrotic tissue in the callus (Figure 2B, Figure S6A). Absence of bone bridging was striking 28 days  
152 post-fracture on microCT scans of *Prss56-Nf1<sup>fl/fl</sup>* and *Prss56-Nf1<sup>fl/-</sup>* mutant calluses and correlated with  
153 fibrotic accumulation (Figure 2C-D, Figure S6). The percentage of bone union was significantly different  
154 between mutant and control mice (p=0.0067) but not between the mutant groups (p=0.52). We  
155 confirmed the fracture nonunion phenotype of *Prss56-Nf1* KO mice using a semi-stabilized fracture  
156 model (Figure S7). Thus, *Nf1* biallelic inactivation in BC-derived pSSPCs and SCs leads to tibial  
157 pseudarthrosis.

158

159 ***Nf1*-deficient BC-derived pSSPCs and Schwann cells contribute to callus fibrosis**

160 We then investigated the identity and fate of BC derivatives in uninjured tibia and fracture callus of  
161 *Prss56-Nf1<sup>+/+</sup>* and *Prss56-Nf1<sup>fl/fl</sup>* mice. We observed an increased percentage of tdTom<sup>+</sup> periosteal cells  
162 in *Prss56-Nf1<sup>fl/fl</sup>* mice compared to control mice, likely due to their increased proliferation. At 14 days  
163 post-injury, tdTom<sup>+</sup> cells were heterogeneously distributed in the fracture callus with regions rich in  
164 tdTom<sup>+</sup> cells and regions without tdTom<sup>+</sup> cells (Figure S8A-B). In *Prss56-Nf1<sup>+/+</sup>* control mice, tdTom<sup>+</sup>  
165 cells were SOX9<sup>+</sup> cartilage cells and OSX<sup>+</sup> bone cells but their contribution to cartilage was decreased

166 in *Prss56-Nf1<sup>fl/fl</sup>* mice (Figure 2E-F, Figure S8C-D). TdTom+ cells were localized in POSTN+ fibrotic  
167 tissue of *Prss56-Nf1<sup>fl/fl</sup>* calluses and corresponded to SOX10+ Schwann cells and *Postn*-expressing  
168 fibroblastic cells (Figure 2G, Figure S8E). TdTom+ Schwann cells in callus fibrosis presented a repair  
169 Schwann cell phenotype as they were positive for the stemness marker SOX2, were negative for the  
170 differentiation marker Myelin Basic Protein (MBP) and were not localized along nerves (Figure 2G).  
171 Although we detected tdTom+ fibrotic cells, the fibrous tissue of *Prss56-Nf1<sup>fl/fl</sup>* calluses was mostly  
172 composed of non-traced cells, indicating that wild-type cells also contributed to callus fibrosis (Figure  
173 S8E). This correlated with NGS results from patient samples, where we observed absence or low  
174 percentage of *NF1*-mutated cells in PA fibrous tissue whereas a high percentage of *NF1* mutated cells  
175 was detected in PA periosteum (Table S2). Hence, *Nf1*-deficient SSPC and SCs from the periosteum,  
176 as well as wild-type cells contribute to callus fibrosis in CPT.

177

#### 178 ***NF1*-deficient periosteal SSPCs adopt a fibrotic fate during bone repair**

179 To explore the impact of *NF1* biallelic loss on the periosteum and pSSPCs, we compared PA periosteum  
180 from patients P5 and P13 with IC periosteum from patients P13 and P15 using single-nucleus RNAseq  
181 (snRNAseq) analyses (Figure 3A, Figure S9A-D). We identified 4 main cell populations:  
182 pericytes/smooth muscle cells (SMCs), endothelial cells, immune cells, and SSPCs/fibroblasts  
183 encompassing three subpopulations expressing *PDGFRA*, *ADAM12/NCAM1* (CD56), and  
184 osteochondral genes (Figure 3B-C, Figure S9D). The percentage of SSPCs/fibroblasts and *ADAM12*+  
185 cells was increased in periosteum from PA site (Figure 3D). In addition, PA periosteum displayed  
186 increased fibrotic, osteogenic, chondrogenic, and cellular responses to TGF $\beta$  lineage scores compared  
187 to IC periosteum, revealing the pro-fibrotic phenotype of pSSPCs in PA periosteum (Figure 3E). We also  
188 observed increased MAPK activation lineage score in PA periosteum, correlated with biallelic *NF1* loss  
189 detected in this tissue. We performed bulk RNAseq analyses of IC and PA primary pSSPCs carrying  
190 *NF1* biallelic inactivation and MAPK overactivation (Figure S10E). We confirmed the pro-fibrotic  
191 phenotype of PA pSSPCs, which overexpressed fibrotic and MAPK-related genes and were enriched  
192 for Gene Ontology related to skeletal development and extracellular matrix (ECM) (Figure S10F-G). We  
193 observed increased proliferation and impaired in vitro chondrogenic differentiation (5/6 patients) of PA  
194 compared to IC pSSPCs (Figure S10H-I) and detected variable effect of *NF1* biallelic inactivation on the  
195 osteogenic and adipogenic differentiation of pSSPCs (Figure S10I). To investigate the impact of *NF1*



196 loss of function on the regenerative potential of pSSPCs, we grafted PA- or IC-derived pSSPCs at the  
197 fracture site of immunodeficient mice (Figure 3F, Figure S10J). PA-derived pSSPCs switched from a  
198 chondrogenic to a fibrotic fate after fracture as they were detected within fibrotic tissue, whereas IC-  
199 derived pSSPCs mostly contributed to cartilage in the fracture callus (Figure 3G). The pro-fibrotic fate  
200 of PA-derived pSSPCs led to an increase of total callus fibrosis and altered bone healing at 28 days  
201 post-injury (Figure 3H). We also observed the fibrotic fate of *Nf1*-deficient pSSPCs in *Prss56-Nf1* KO  
202 mice. We grafted periosteum or cultured pSSPCs from *Prss56-Nf1<sup>fl/fl</sup>* mutant or *Prss56-Nf1<sup>+/+</sup>* control  
203 mice at the fracture site of wild-type hosts (Figure 3I, Figure S11A-G). Although the contribution to the  
204 callus was equivalent (Figure S11H), we observed a reduced contribution to cartilage of mutant  
205 compared to control tdTom<sup>+</sup> periosteum or pSSPCs. These tdTom<sup>+</sup> mutant cells were present in callus  
206 fibrosis, indicating a fate change of *Nf1*-deficient pSSPCs during bone repair (Figure 3I). In sum, *NF1*  
207 biallelic inactivation causes fibrotic differentiation of pSSPCs in response to bone fracture.

208

#### 209 **Fibrotic differentiation of *Nf1*-deficient pSSPCs is due to over activation of MAPK pathway**

210 To uncover the molecular mechanisms underlying pSSPC fate conversion, we first investigated the role  
211 of the MAPK pathway during the early response of pSSPCs to bone fracture. We analyzed snRNAseq  
212 datasets from uninjured periosteum, and from injured periosteum and hematoma/callus at days 3, 5 and  
213 7 post-fracture in wild-type mice (16) (Fig 4A). SSPCs activate in 3 successive phases: a  
214 stem/progenitor phase predominant in the uninjured dataset, an injury-induced fibrogenic phase  
215 predominant at day 5 post-fracture, and a bifurcation between osteogenesis and chondrogenesis,  
216 predominant at day 7 post-fracture (Figure 4B). We assessed the MAPK pathway activation during these  
217 3 phases using a MAPK score based on the expression profile of MAPK target genes. Along  
218 pseudotime, we observed an increase of MAPK score between the SSPC and fibrogenic stages,  
219 followed by a decrease when cells engage into osteochondral lineage (Figure 4C). MAPK score was  
220 reduced in cells with high chondrogenic lineage score and *Sox9* expression but remained constant in  
221 cells with a high osteogenic lineage score (Figure 4D). This showed that pSSPCs specifically  
222 downregulate the MAPK pathway to transition from the fibrogenic to the chondrogenic stage. Co-  
223 immunostaining for the chondrogenic marker SOX9 and pERK on day 7 wild-type callus sections  
224 confirmed a negative correlation between SOX9 and pERK signals (Figure 4E). Analyses in tdTom<sup>+</sup>  
225 cells showed higher pERK and reduced SOX9 signals in *Prss56-Nf1<sup>fl/fl</sup>* compared to *Prss56-Nf1<sup>+/+</sup>*

226 calluses. In tdTom+ *Prss56-Nf1<sup>+/+</sup>* cells, we observed a negative correlation between pERK and SOX9  
227 signals whereas tdTom+ *Prss56-Nf1<sup>fl/fl</sup>* cells only exhibited high pERK and low SOX9 signals (Figure  
228 4F). The fibrotic fate of *Nf1*-deficient pSSPCs is therefore caused by overactivation of MAPK signaling,  
229 which prevents the transition from fibrogenic to chondrogenic stage required for callus formation.

230

### 231 ***Nf1*-deficient Schwann cells are the main driver of fibrosis in CPT**

232 Because the fibrotic tissue at the pseudarthrosis site was also composed of wild-type cells in both  
233 patients with CPT and *Prss56-Nf1* KO mice, we explored the role of the mutant fracture environment on  
234 SSPC fate. Transplanted wild-type GFP+ pSSPCs became fibrotic in the callus of *Prss56-Nf1<sup>fl/fl</sup>* but not  
235 *Prss56-Nf1<sup>+/+</sup>* hosts (Figure S11I), showing the pro-fibrotic influence of the mutant callus environment.  
236 We investigated the role of *Nf1*-deficient pSSPCs and SCs in this deleterious paracrine effect. Although  
237 transplanted *Nf1*-deficient pSSPCs induced callus fibrosis in wild-type hosts, this fibrotic tissue was  
238 resorbed, and bone bridging was apparent by 28 days post-fracture (Figure S11F-G). In contrast,  
239 transplantation of *Nf1*-deficient Schwann cells at the fracture site of wild-type hosts induced tibial  
240 pseudarthrosis with absence of bone bridging and fibrous accumulation at both 14 and 28 days post-  
241 fracture (Figure 5A). *Nf1*-deficient Schwann cells are therefore the main driver of fibrotic accumulation  
242 in tibial pseudarthrosis. We generated snRNAseq datasets of day 7 post-fracture periosteum and callus  
243 of *Prss56-Nf1<sup>fl/fl</sup>* mice and performed integration with day 7 control dataset (Figure 5B, Fig S12A-D).  
244 Given the rarity of tdTom+ cells, *Prss56-Nf1<sup>fl/fl</sup>* dataset was composed solely of non-traced (i.e., wild-  
245 type) cells in mutant environment (Figure S12E). We observed a reduced proportion of cells in  
246 chondrogenic clusters and increased proportion of cells in fibrogenic clusters in mutant compared to  
247 control dataset (Figure 5C-D). This indicated that wild-type pSSPCs in the mutant environment are partly  
248 retained in the fibrogenic stage.

249 We sought to identify the factors driving the pro-fibrotic effect of *Nf1*-deficient Schwann cells on SSPCs.  
250 We observed that tdTom+ Schwann cells in the fibrotic tissue of *Prss56-Nf1<sup>fl/fl</sup>* mice expressed *Tgfb1*,  
251 Oncostatin M (*Osm*) and *Pdgfa* (Fig. 5E), factors previously shown to be secreted by repair SCs during  
252 tissue repair (35, 36). In depth analyses of cluster 6 from the snRNAseq data, corresponding to pSSPCs  
253 transitioning from the fibrogenic to the chondrogenic stage, showed an upregulation of GO terms related  
254 to TGF $\beta$  specifically in *Prss56-Nf1<sup>fl/fl</sup>* dataset (Figure S13). This correlated with increased *Tgfb1*  
255 expression and an increased percentage of phospho-SMAD2 (TGF $\beta$  downstream effector)-positive cells

256 in day 7 *Prss56-Nf1<sup>fl/fl</sup>* compared to *Prss56-Nf1<sup>+/+</sup>* calluses (Figure 5F-G). To confirm the role of TGFβ  
257 in the pro-fibrotic effect of *Nf1*-deficient Schwann cells, we treated wild-type mice grafted with tdTom+  
258 *Prss56-Nf1<sup>fl/fl</sup>* Schwann cells or *Prss56-Nf1<sup>fl/fl</sup>* mice with TGFβ blocking antibody (Figure 5H). We  
259 observed decreased fibrosis in the callus of treated compared to control mice. *Prss56-Nf1<sup>fl/fl</sup>* mice treated  
260 with TGFβ blocking antibody exhibited bone bridging and improved union score at day 28 post-fracture  
261 (Figure 5I), indicating that TGFβ is one of the factors mediating the pro-fibrotic effect of *Nf1*-deficient  
262 Schwann cells in tibial pseudarthrosis.

263

### 264 **Combined MEK and SHP2 inhibition prevents tibial pseudarthrosis**

265 To develop therapeutic approaches for CPT, we aimed to reduce the pro-fibrotic effects of *NF1* mutant  
266 pSSPCs and SCs by inhibiting RAS-MAPK overactivation. We tested the efficacy of MEK inhibition using  
267 selumetinib, SHP2 inhibition using SHP099, and the combination of MEK and SHP2 inhibitors to block  
268 RAS-MAPK overactivation and prevent CPT. We first tested the impact of MEK with or without SHP2  
269 inhibition on MAPK activation in *NF1*-deficient pSSPCs from patients with CPT. We observed a  
270 substantial reduction of MAPK activation from 1 μM with combined treatment but not with single  
271 treatment compared to DMSO-treated cells (Fig 6A-B). Combined MEK-SHP2 inhibition significantly  
272 reduced in vitro proliferation and increased chondrogenic differentiation of *NF1*-deficient pSSPCs  
273 compared to DMSO-treated cells (Figure 6C-D). As *Prss56-Nf1* KO mice faithfully recapitulate the bone  
274 repair defect observed in CPT, we tested the benefit of MEK-SHP2 inhibition on this relevant preclinical  
275 model of CPT by treating daily *Prss56-Nf1<sup>fl/-</sup>* mice with selumetinib, SHP099, combined selumetinib and  
276 SHP099, or vehicle (Figure 6E). Whereas control mice did not show bone union, mice treated with  
277 combined selumetinib and SHP099 displayed an 83% union rate (Figure 6F-G), demonstrating  
278 treatment efficacy in preventing pseudarthrosis. Selumetinib treatment alone had a mild effect on union  
279 rate and SHP099 treatment alone was not as efficient as combined treatment (25% and 60% of union  
280 rate respectively, Figure 6G). Combined MEK-SHP2 inhibition was the only treatment leading to  
281 increased callus, cartilage, and bone formation and reduced fibrosis accumulation (Figure 6H).  
282 Furthermore, analysis of tdTom+ cells in the fracture callus showed that combined treatment corrects  
283 *Nf1*-deficient cell fate impairment, as tdTom+ cells formed cartilage instead of fibrosis in *Prss56-Nf1*  
284 mutant mice treated with both SHP099 and selumetinib compared to untreated mutant mice (Figure 6I).  
285 We confirmed that the combined treatment was also efficacious in the *Prx1-Nf1* KO model, in which the

286 pseudarthrosis phenotype results from *Nf1* inactivation in all pSSPCs (Fig. S14). Overall, combined  
287 MEK-SHP2 inhibition efficiently prevented fibrous accumulation and pseudarthrosis, demonstrating its  
288 promising therapeutic potential.

289 **Discussion**  
290

291 In this study, we uncover the cellular origin and underlying molecular mechanisms of CPT,  
292 demonstrating that SSPCs and Schwann cells are the affected cell types in CPT. We detected *NF1*  
293 biallelic inactivation in SSPCs and Schwann cells and increased numbers of pERK+ SSPCs and  
294 Schwann cells in pathological periosteum of patients with CPT. These findings correlate with the  
295 presence of *Nf1*-deficient SSPCs and Schwann cells in the periosteum and fibrous callus of *Prss56-Nf1*  
296 *KO* mice that exhibit tibial pseudarthrosis. Functionally, human and murine *NF1*-deficient pSSPCs in  
297 both *Prss56-Nf1* *KO* and *Prx1-Nf1* *KO* mouse models displayed a pro-fibrotic phenotype and contributed  
298 to callus fibrosis. The role of MAPK signaling in regulating SSPC differentiation is unclear, as previous  
299 studies showed beneficial and deleterious effect of MAPK cascade in chondrogenesis (37–42). Using  
300 snRNAseq, we established the temporal dynamics of MAPK signaling required during pSSPC activation  
301 and differentiation in response to fracture. MAPK signaling is first up-regulated in pSSPCs that transition  
302 from a stem/progenitor stage to an injury-induced fibrogenic stage and is down-regulated during the  
303 transition from fibrogenesis to chondrogenesis. These results provide the molecular mechanism  
304 explaining the retention of *NF1*-deficient pSSPCs in the fibrogenic state as they fail to downregulate  
305 MAPK signaling due to *NF1* loss of function. Consequently, fibrotic pSSPCs accumulate in the center  
306 of the callus and interfere with fracture consolidation. These results may have a broader impact in  
307 understanding other fibrotic bone repair disorders sharing similar mechanisms with CPT.

308  
309 Most strikingly, we demonstrate that *NF1* biallelic inactivation in CPT is not restricted to the skeletal  
310 lineage. Our results highlight the pivotal role of Schwann cells (SCs), a neural cell type, in promoting  
311 callus fibrosis in CPT. We identified *NF1*-deficient SCs as the source of pro-fibrotic factors causing tibial  
312 pseudarthrosis in *Prss56-Nf1* *KO* mice. Although *Nf1*-deficient pSSPCs exert a pro-fibrotic effect, SCs  
313 are the main fibrotic drivers in CPT recruiting wild type pSSPCs to contribute also to callus fibrosis. SCs  
314 in the fibrous callus of *Prss56-Nf1* *KO* mice exhibit a repair SC phenotype. Previous studies showed that  
315 MAPK pathway regulates the transition from SCs to repair SCs suggesting that *Nf1*-deficient SCs are  
316 blocked in a repair SC state and maintain the secretion of pro-fibrotic factors in CPT (43–45). We  
317 identified that *Nf1*-deficient SCs express several profibrotic factors including TGF $\beta$ , OSM, and PDGF-  
318 AA and that inhibiting TGF $\beta$  improved healing in *Prss56-Nf1* *KO* mice. This study provides evidence  
319 that SCs can interfere with the repair process of non-peripheral nervous tissues and promote fibrotic

320 tissue accumulation. Whereas previous studies highlighted the key paracrine role of SCs in skin and  
321 digit tip regeneration, the involvement of SCs and peripheral nerves in tissue repair dysfunctions and  
322 fibrotic disorders remains understudied (35, 36, 46).

323

324 The involvement of both pSSPCs and SCs in CPT reveals mechanisms for NF1 bone manifestations.  
325 CPT and other NF1 bone phenotypes have been investigated independent of other NF1 symptoms,  
326 presumably because the cell types involved have distinct embryonic origins. SCs and melanocytes,  
327 responsible for NFBs and CALMs, are neural crest-derived, whereas axial and appendicular bones are  
328 derived from the mesoderm. Our genetic analysis of the *NF1* mutational landscape in CPT revealed that  
329 *NF1* 2<sup>nd</sup> hit occurs early during embryonic development and is not restricted to the skeletal lineage. In  
330 addition, we detected the same 2 *NF1* hits in SSPCs and SCs in pathological periosteum of one patient  
331 with CPT, showing that both affected cell types share a common origin. In mice, we identified BCs as a  
332 population giving rise to SCs and pSSPCs in long bones and showed that *Nf1* loss in these derivatives  
333 cause pseudarthrosis. This shows that BCs are the cellular origin of CPT in mice, and presumably in  
334 NF1 patients. The *Prss56-Nf1* KO model is the first relevant model to faithfully recapitulate the variability  
335 of NF1 symptoms, demonstrating that CPT shares a common BC origin with NFBs and CALMs (24). In  
336 addition to sharing a common cellular origin, we further reveal that CPTs and NFBs share common  
337 pathogenic mechanisms. In NFBs, *Nf1*-deficient SCs also secrete profibrotic factors, including TGFβ  
338 and SCF, to promote fibroblast accumulation and proliferation involved in tumor progression (47–49).  
339 Our study thus highlights the parallels between NF1 symptoms and calls for more integrated analysis of  
340 NF1 features.

341

342 Beside unraveling the pathogenic bases of CPT, we demonstrate the relevance of the *Prss56-Nf1* KO  
343 mouse model as a preclinical model for CPT-related fibrous nonunion. Because NF1 symptoms share  
344 common pathogenic mechanisms, we considered therapeutical strategies developed for tumoral  
345 manifestations and showed that they can also be considered for CPT treatment. Selumetinib is FDA-  
346 approved for inoperable neurofibroma yet did not reveal substantial effects in previous mouse models  
347 of NF1 bone manifestations (19, 32, 50). Therefore, we tested the combination of MEK and SHP2  
348 inhibitors to counteract the pro-fibrotic effects of *NF1*-deficient pSSPCs and SCs. We observed a  
349 therapeutic effect of the selumetinib/SHP099 combination with efficient MAPK inhibition in *NF1*-deficient

350 pSSPCs and restoration of the in vitro proliferation and differentiation potential of human pSSPCs. In  
351 vivo treatment of *Prss56-Nf1* KO or *Prx1-Nf1* KO mice showed promising results, with bone union  
352 reached in 83% and 100% of callus respectively, concomitant with a drastic decrease in fibrotic  
353 accumulation one month after fracture. The effect of a 10-day oral treatment opens the door to clinical  
354 strategies for CPT overcoming potential tolerability issues of combining SHP2 and MEK inhibitors. In  
355 addition, the possibility of using local delivery to minimize these issues could also be tested. These  
356 results represent a potential breakthrough in improving the prognosis for CPT patients.

357

358 There are limitations to this study. CPT is extremely rare (1/150 000 individuals) and patients undergo  
359 surgical treatment at a young age (first surgery at  $3.1 \pm 1$  years-old). Thus, obtaining periosteum samples  
360 of patients with CPT is challenging and only small amounts of tissues can be collected. This strongly  
361 limits our ability to isolate rare cell populations, including SCs, for extensive analysis. Similarly, in  
362 *Prss56-Nf1* KO mice, BC derivatives represent a rare subset of cells in intact periosteum and in the  
363 callus after fracture. This highlights the strong paracrine effect of *Nf1*-deficient cells but makes it  
364 challenging to isolate BC-derived cells to further explore the impact of *Nf1* loss of function in these cells.  
365 Last, the *Prss56-Nf1* KO mouse model recapitulates the fibrous nonunion phenotype, but not congenital  
366 tibial bowing, which might suggest independent mechanisms and require further studies.

## 367 **Materials and Methods**

368

### 369 **Study design**

370 In our study, we aimed to understand the mechanisms causing CPT. We combined the analyses of  
371 samples from patients undergoing surgery for CPT with the analyses of the relevant *Prss56-Nf1* KO  
372 mouse model. For the human cohort, we collected tissues from patients operated for CPT at Necker-  
373 Enfants Malades hospital during this study and formal consent was obtained. For each patient, the  
374 affected PA tissue was compared with non-affected IC tissue. Two patients undergoing reintervention  
375 were excluded from the cohort as original PA tissues from the first resection were not accessible and  
376 we did not detect *NF1* biallelic inactivation. Therefore, we could not conclude on the presence/absence  
377 of *NF1* mutation. For the mouse study, all animals used for the study were included except samples with  
378 distal or proximal fractures that can affect bone repair. No outliers were excluded from the study. Based  
379 on our previous publications (12, 13, 51), groups of 3 to 7 samples are sufficient to assess statistical  
380 differences between groups. The n for individual experiments is indicated in the figure legends. Every  
381 group is composed of samples from at least 2 independent experiments. For both human and mouse  
382 studies, samples were assigned a unique sample number for blinded analyses. No randomization  
383 methods were used for the study, as groups were homogeneous and composed of equivalent animals  
384 based on gender, age, and genotype.

385

### 386 **Human tissue sample collection**

#### 387 *Cohort and ethical approval*

388 Sample collection from patients affected by congenital pseudarthrosis of the tibia (CPT) was performed  
389 at Necker-Enfants Malades Hospital, Paris. This study was approved by the Ethics Committee CPP-  
390 IDF-2 (#ID-RCB/EUDRACT: 2014- A01420-47; IMNIS2014-03). Informed consent of legal  
391 representatives of patients was obtained prior to sample collection. The cohort was composed of 17  
392 patients, 7 diagnosed with *NF1*-associated CPT and 10 with isolated CPT. *NF1* diagnosis was  
393 performed by the Dermatology department at Necker-Enfants Malades Hospital, following guidelines  
394 from International Consensus Group on Neurofibromatosis Diagnostic Criteria. Isolated CPT was  
395 defined by the absence of additional *NF1* clinical feature and the absence of *NF1* pathogenic variant in  
396 blood sample. 14 patients were treated for the first time (named “Primary” operation in Table S1) and 3



397 were undergoing additional surgery following initial treatment (named “Reintervention”). Detailed  
398 information about patient age, gender, NF1 diagnosis, type of operation and affected bones are reported  
399 in Table S1.

400

#### 401 *Sample collection*

402 Tissues were collected during CPT treatment surgery using the induced membrane technique typically  
403 performed in 2 steps (52). The first surgical procedure consists of pseudarthrosis tissue resection,  
404 intramedullary nailing, and insertion of a cement spacer to fill the gap. During this procedure, affected  
405 periosteum, bone marrow, bone, fibrous tissue, muscle, and skin from the PA site were collected. For  
406 patients undergoing surgery as secondary treatment, the primary pseudarthrosis tissues were  
407 unavailable but were collected adjacent to the primary PA site when possible. After 6 to 8 weeks, a  
408 second surgical procedure was performed to remove the cement spacer and graft autologous iliac crest  
409 periosteum and cancellous bone in the induced membrane that formed around the cement. During this  
410 second procedure, unaffected periosteum and spongy bone from the iliac crest (IC) were harvested. A  
411 blood sample was also collected during surgery. Tissue dissection and identification was performed by  
412 orthopedic surgeons. Collected tissues were immediately placed in DMEM (21063029, ThermoFischer  
413 Scientific) with 10% HEPES (15630056, ThermoFischer Scientific) and 1% Penicillin-Streptomycin  
414 (15140122, ThermoFischer Scientific) at 4°C, and processed for *NF1* genotyping, single-nuclei RNAseq,  
415 primary culture and histological analyses as described below.

416

#### 417 **Mice**

418 C57BL/6ScNj, *Prx1<sup>Cre</sup>* (IMSR\_JAX:005584) (53), *Rosa26-mtdTomato-mEGFP* (*R26<sup>mTmG</sup>*)  
419 (IMSR\_JAX:007676) (54), *R26tdTomato* (*R26<sup>tdTom</sup>*) (IMSR\_JAX:007914) (55), *Nf1<sup>flox</sup>* (*Nf1<sup>fl</sup>*)  
420 (IMSR\_JAX:017640), *Nf1*-knock out (*Nf1<sup>-</sup>*) (56) were obtained from Jackson Laboratory. *Prss56<sup>Cre</sup>* mice  
421 were generated by Piotr Topilko (24, 25). Immunodeficient nude CD1 mice were purchased from Janvier  
422 Labs. Mice were bred in animal facilities at IMRB, Creteil and Imagine Institute, Paris. Two to five mice  
423 were kept in separated ventilated cages, in a pathogen-controlled environment with 12:12-hour  
424 light:dark cycles and ad libitum access to water and food. All procedures performed were approved by  
425 Paris University or Paris Est Creteil University Ethical Committees (#2795-201506051048131, #19295-  
426 2019052015468705, #27181-202009141201846, #33818-2021110818301267). Males and females

427 were mixed in experimental groups. No specific randomization method was used. Bone injury and tissue  
428 collection for graft and digestion were performed on 10- to 14-week-old mice. Six- to 8-week-old mice  
429 were used for primary periosteum culture. Controlled breeding was performed to collect embryonic  
430 tissues at 12.5, 13.5, and 14.5 days of development. Samples were labeled at the time of tissue  
431 collection and using a labeling system allowing blind analyses in all experiments.

432

### 433 **Statistical analyses**

434 Data are reported as mean +/- standard deviation. n represents the number of samples used for the  
435 analysis. For human experiments, each sample corresponds to a different patient. For mouse  
436 experiments, each sample corresponds to an individual mouse. Statistical differences between  
437 experimental groups were evaluated using GraphPad Prism. For comparison between 2 groups, two-  
438 side Mann-Whitney test was used. For comparison between 3 or 4 groups, one-way ANOVA followed  
439 by Holm-Šídák's multiple comparisons post-hoc test was used. The comparison in bone bridging  
440 between mutants and control groups was performed using Chi-squared test. For SOX9/pERK signal  
441 correlation, each value corresponds to an individual cell. Correlation analysis and simple linear  
442 regression were performed to assess the correlation between both signals. Significance was determined  
443 as \*p < 0.05, \*\*p < 0.01, \*\*\*p < 0.001, \*\*\*\*p < 0.0001. All experiments were performed in at least 2  
444 independent experiments.

445

### 446 **List of Supplementary Materials**

447

448 Material and Methods

449 Figure S1 to Figure S14

450 Table S1 to Table S6

451 MDAR checklist

452 Data File S1

453 **References**

- 454 1. S. Pannier, Congenital pseudarthrosis of the tibia. *Orthopaedics & Traumatology: Surgery & Research*  
455 **97**, 750–761 (2011).
- 456 2. M. J. Siebert, C. A. Makarewich, Anterolateral Tibial Bowing and Congenital Pseudoarthrosis of the  
457 Tibia: Current Concept Review and Future Directions. *Curr Rev Musculoskelet Med* **15**, 438–446 (2022).
- 458 3. D. H. Gutmann, R. E. Ferner, R. H. Listernick, B. R. Korf, P. L. Wolters, K. J. Johnson,  
459 Neurofibromatosis type 1. *Nat Rev Dis Primers* **3**, 17004 (2017).
- 460 4. I. Eisenbarth, G. Assum, D. Kaufmann, W. Krone, Evidence for the presence of the second allele of  
461 the neurofibromatosis type 1 gene in melanocytes derived from café au lait macules of NF1 patients.  
462 *Biochem Biophys Res Commun* **237**, 138–141 (1997).
- 463 5. L. Kluwe, R. Friedrich, V. F. Mautner, Loss of NF1 allele in Schwann cells but not in fibroblasts derived  
464 from an NF1-associated neurofibroma. *Genes Chromosomes Cancer* **24**, 283–285 (1999).
- 465 6. L. Q. Le, C. Liu, T. Shipman, Z. Chen, U. Suter, L. F. Parada, Susceptible stages in Schwann cells  
466 for NF1-associated plexiform neurofibroma development. *Cancer Res* **71**, 4686–4695 (2011).
- 467 7. J. Wu, J. P. Williams, T. A. Rizvi, J. J. Kordich, D. Witte, D. Meijer, A. O. Stemmer-Rachamimov, J.  
468 A. Cancelas, N. Ratner, Plexiform and dermal neurofibromas and pigmentation are caused by Nf1 loss  
469 in desert hedgehog-expressing cells. *Cancer Cell* **13**, 105–116 (2008).
- 470 8. Y. Zhu, P. Ghosh, P. Charnay, D. K. Burns, L. F. Parada, Neurofibromas in NF1: Schwann cell origin  
471 and role of tumor environment. *Science* **296**, 920–922 (2002).
- 472 9. B. Hermanns-Sachweh, J. Senderek, J. Alfer, B. Klosterhalfen, R. Büttner, L. Füzesi, M. Weber,  
473 Vascular changes in the periosteum of congenital pseudarthrosis of the tibia. *Pathol Res Pract* **201**,  
474 305–312 (2005).
- 475 10. D. A. Stevenson, H. Zhou, S. Ashrafi, L. M. Messiaen, J. C. Carey, J. L. D’Astous, S. D. Santora, D.  
476 H. Viskochil, Double inactivation of NF1 in tibial pseudarthrosis. *Am J Hum Genet* **79**, 143–148 (2006).
- 477 11. C. Brekelmans, S. Hollants, C. De Groote, N. Sohier, M. Maréchal, L. Geris, F. P. Luyten, L.  
478 Ginckels, R. Sciot, T. de Ravel, L. De Smet, J. Lammens, E. Legius, H. Brems, Neurofibromatosis type  
479 1-related pseudarthrosis: Beyond the pseudarthrosis site. *Hum Mutat* **40**, 1760–1767 (2019).
- 480 12. O. Duchamp de Lageneste, A. Julien, R. Abou-Khalil, G. Frangi, C. Carvalho, N. Cagnard, C.  
481 Cordier, S. J. Conway, C. Colnot, Periosteum contains skeletal stem cells with high bone regenerative  
482 potential controlled by Periostin. *Nat Commun* **9**, 773 (2018).
- 483 13. A. Julien, S. Perrin, E. Martínez-Sarrà, A. Kanagalingam, C. Carvalho, M. Luka, M. Ménager, C.

484 Colnot, Skeletal stem/progenitor cells in periosteum and skeletal muscle share a common molecular  
485 response to bone injury. *J of Bone & Mineral Res* , jbmr.4616 (2022).

486 14. Z. Li, C. A. Meyers, L. Chang, S. Lee, Z. Li, R. Tomlinson, A. Hoke, T. L. Clemens, A. W. James,  
487 Fracture repair requires TrkA signaling by skeletal sensory nerves. *Journal of Clinical Investigation* **129**,  
488 5137–5150 (2019).

489 15. B. G. Matthews, S. Novak, F. V. Sbrana, J. L. Funnell, Y. Cao, E. J. Buckels, D. Grcevic, I. Kalajzic,  
490 Heterogeneity of murine periosteum progenitors involved in fracture healing. *eLife* **10**, e58534 (2021).

491 16. S. Perrin, C.-A. Wotawa, V. Bretegnier, M. Luka, F. Culpier, C. Masson, M. Ménager, C. Colnot,  
492 Single nuclei transcriptomics reveal the differentiation trajectories of periosteal skeletal/stem progenitor  
493 cells in bone regeneration (2024), doi:10.7554/eLife.92519.1.

494 17. N. van Gastel, S. Stegen, G. Eelen, S. Schoors, A. Carlier, V. W. Daniëls, N. Baryawno, D.  
495 Przybylski, M. Depypere, P.-J. Stiers, D. Lambrechts, R. Van Looveren, S. Torrekens, A. Sharda, P.  
496 Agostinis, D. Lambrechts, F. Maes, J. V. Swinnen, L. Geris, H. Van Oosterwyck, B. Thienpont, P.  
497 Carmeliet, D. T. Scadden, G. Carmeliet, Lipid availability determines fate of skeletal progenitor cells via  
498 SOX9. *Nature* **579**, 111–117 (2020).

499 18. J. Sales de Gauzy, F. Fitoussi, J.-L. Jouve, C. Karger, A. Badina, A.-C. Masquelet, Traumatic  
500 diaphyseal bone defects in children. *Orthopaedics & Traumatology: Surgery & Research* **98**, 220–226  
501 (2012).

502 19. J. de la Croix Ndong, D. M. Stevens, G. Vignaux, S. Uppuganti, D. S. Perrien, X. Yang, J. S. Nyman,  
503 E. Harth, F. Elefteriou, Combined MEK Inhibition and BMP2 Treatment Promotes Osteoblast  
504 Differentiation and Bone Healing in *Nf1*<sup>osx<sup>-/-</sup></sup> Mice: RAS/ERK SIGNALING IN OSTEOPROGENITORS.  
505 *J Bone Miner Res* **30**, 55–63 (2015).

506 20. T. El Khassawna, D. Toben, M. Kolanczyk, K. Schmidt-Bleek, I. Koennecke, H. Schell, S. Mundlos,  
507 G. N. Duda, Deterioration of fracture healing in the mouse model of NF1 long bone dysplasia. *Bone* **51**,  
508 651–660 (2012).

509 21. N. Kamiya, R. Yamaguchi, O. Aruwajoye, A. J. Kim, G. Kuroyanagi, M. Phipps, N. S. Adapala, J. Q.  
510 Feng, H. K. Kim, Targeted Disruption of *NF1* in Osteocytes Increases FGF23 and Osteoid With  
511 Osteomalacia-like Bone Phenotype: NF1 DISRUPTION IN OSTEOCYTES CAUSES A  
512 MINERALIZATION DEFECT. *J Bone Miner Res* **32**, 1716–1726 (2017).

513 22. R. Sharma, X. Wu, S. D. Rhodes, S. Chen, Y. He, J. Yuan, J. Li, X. Yang, X. Li, L. Jiang, E. T. Kim,

514 D. A. Stevenson, D. Viskochil, M. Xu, F.-C. Yang, Hyperactive Ras/MAPK signaling is critical for tibial  
515 nonunion fracture in neurofibromin-deficient mice. *Human Molecular Genetics* **22**, 4818–4828 (2013).

516 23. W. Wang, J. S. Nyman, K. Ono, D. A. Stevenson, X. Yang, F. Elefteriou, Mice lacking Nf1 in  
517 osteochondroprogenitor cells display skeletal dysplasia similar to patients with neurofibromatosis type  
518 I. *Human Molecular Genetics* **20**, 3910–3924 (2011).

519 24. K. J. Radomska, F. Couplier, A. Gresset, A. Schmitt, A. Debliche, S. Lemoine, P. Wolkenstein, J.-  
520 M. Vallat, P. Charnay, P. Topilko, Cellular Origin, Tumor Progression, and Pathogenic Mechanisms of  
521 Cutaneous Neurofibromas Revealed by Mice with Nf1 Knockout in Boundary Cap Cells. *Cancer Discov*  
522 **9**, 130–147 (2019).

523 25. A. Gresset, F. Couplier, G. Gerschenfeld, A. Jourdon, G. Matesic, L. Richard, J.-M. Vallat, P.  
524 Charnay, P. Topilko, Boundary Caps Give Rise to Neurogenic Stem Cells and Terminal Glia in the Skin.  
525 *Stem Cell Reports* **5**, 278–290 (2015).

526 26. S. Ahsan, Y. Ge, M. A. Tainsky, Combinatorial therapeutic targeting of BMP2 and MEK-ERK  
527 pathways in NF1-associated malignant peripheral nerve sheath tumors. *Oncotarget* **7**, 57171–57185  
528 (2016).

529 27. E. Dombi, A. Baldwin, L. J. Marcus, M. J. Fisher, B. Weiss, A. Kim, P. Whitcomb, S. Martin, L. E.  
530 Aschbacher-Smith, T. A. Rizvi, J. Wu, R. Ershler, P. Wolters, J. Therrien, J. Glod, J. B. Belasco, E.  
531 Schorry, A. Brofferio, A. J. Starosta, A. Gillespie, A. L. Doyle, N. Ratner, B. C. Widemann, Activity of  
532 Selumetinib in Neurofibromatosis Type 1-Related Plexiform Neurofibromas. *N Engl J Med* **375**, 2550–  
533 2560 (2016).

534 28. D. Casey, S. Demko, A. Sinha, P. S. Mishra-Kalyani, Y.-L. Shen, S. Khasar, M. A. Goheer, W. S.  
535 Helms, L. Pan, Y. Xu, J. Fan, R. Leong, J. Liu, Y. Yang, K. Windsor, M. Ou, O. Stephens, B. Oh, G. H.  
536 Reaman, A. Nair, S. S. Shord, V. Bhatnagar, S. R. Daniels, S. Sickafuse, K. B. Goldberg, M. R. Theoret,  
537 R. Pazdur, H. Singh, FDA Approval Summary: Selumetinib for Plexiform Neurofibroma. *Clin Cancer Res*  
538 **27**, 4142–4146 (2021).

539 29. A. M. Gross, E. Dombi, P. L. Wolters, A. Baldwin, A. Dufek, K. Herrera, S. Martin, J. Derdak, K. S.  
540 Heisey, P. M. Whitcomb, S. M. Steinberg, D. J. Venzon, M. J. Fisher, A. R. Kim, M. Bornhorst, B. D.  
541 Weiss, J. O. Blakeley, M. A. Smith, B. C. Widemann, Long-Term Safety and Efficacy of Selumetinib in  
542 Children with Neurofibromatosis Type 1 on a Phase 1/2 Trial for Inoperable Plexiform Neurofibromas.  
543 *Neuro Oncol* , noad086 (2023).

544 30. G. S. Baht, P. Nadesan, D. Silkstone, B. A. Alman, Pharmacologically targeting beta-catenin for NF1  
545 associated deficiencies in fracture repair. *Bone* **98**, 31–36 (2017).

546 31. N. Deo, T. L. Cheng, K. Mikulec, L. Peacock, D. G. Little, A. Schindeler, Improved union and bone  
547 strength in a mouse model of NF1 pseudarthrosis treated with recombinant human bone morphogenetic  
548 protein-2 and zoledronic acid: rhBMP-2 AND ZA FOR NF1 PSEUDARTHROSIS. *J. Orthop. Res.* (2017),  
549 doi:10.1002/jor.23672.

550 32. W. Wang, J. S. Nyman, H. E. Moss, G. Gutierrez, G. R. Mundy, X. Yang, F. Elefteriou, Local low-  
551 dose lovastatin delivery improves the bone-healing defect caused by Nf1 loss of function in osteoblasts.  
552 *J Bone Miner Res* **25**, 1658–1667 (2010).

553 33. J. Cai, S. Jacob, R. Kurupi, K. M. Dalton, C. Coon, P. Greninger, R. K. Egan, G. T. Stein, E. Murchie,  
554 J. McClanaghan, Y. Adachi, K. Hirade, M. Dozmorov, J. Glod, S. A. Boikos, H. Ebi, H. Hao, G.  
555 Caponigro, C. H. Benes, A. C. Faber, High-risk neuroblastoma with NF1 loss of function is targetable  
556 using SHP2 inhibition. *Cell Rep* **40**, 111095 (2022).

557 34. J. Wang, K. Pollard, A. N. Allen, T. Tomar, D. Pijnenburg, Z. Yao, F. J. Rodriguez, C. A. Pratilas,  
558 Combined Inhibition of SHP2 and MEK Is Effective in Models of NF1-Deficient Malignant Peripheral  
559 Nerve Sheath Tumors. *Cancer Res* **80**, 5367–5379 (2020).

560 35. A. P. W. Johnston, S. A. Yuzwa, M. J. Carr, N. Mahmud, M. A. Storer, M. P. Krause, K. Jones, S.  
561 Paul, D. R. Kaplan, F. D. Miller, Dedifferentiated Schwann Cell Precursors Secreting Paracrine Factors  
562 Are Required for Regeneration of the Mammalian Digit Tip. *Cell Stem Cell* **19**, 433–448 (2016).

563 36. V. Parfejevs, J. Debbache, O. Shakhova, S. M. Schaefer, M. Glausch, M. Wegner, U. Suter, U.  
564 Riekstina, S. Werner, L. Sommer, Injury-activated glial cells promote wound healing of the adult skin in  
565 mice. *Nat Commun* **9**, 236 (2018).

566 37. B. E. Bobick, W. M. Kulyk, MEK-ERK signaling plays diverse roles in the regulation of facial  
567 chondrogenesis. *Exp Cell Res* **312**, 1079–1092 (2006).

568 38. B. E. Bobick, W. M. Kulyk, The MEK-ERK signaling pathway is a negative regulator of cartilage-  
569 specific gene expression in embryonic limb mesenchyme. *J Biol Chem* **279**, 4588–4595 (2004).

570 39. J. Li, Z. Zhao, J. Liu, N. Huang, D. Long, J. Wang, X. Li, Y. Liu, MEK/ERK and p38 MAPK regulate  
571 chondrogenesis of rat bone marrow mesenchymal stem cells through delicate interaction with TGF-  
572 beta1/Smads pathway. *Cell Prolif* **43**, 333–343 (2010).

573 40. S. Murakami, M. Kan, W. L. McKeenan, B. de Crombrughe, Up-regulation of the chondrogenic

574 Sox9 gene by fibroblast growth factors is mediated by the mitogen-activated protein kinase pathway.  
575 *Proc Natl Acad Sci U S A* **97**, 1113–1118 (2000).

576 41. C. D. Oh, S. H. Chang, Y. M. Yoon, S. J. Lee, Y. S. Lee, S. S. Kang, J. S. Chun, Opposing role of  
577 mitogen-activated protein kinase subtypes, erk-1/2 and p38, in the regulation of chondrogenesis of  
578 mesenchymes. *J Biol Chem* **275**, 5613–5619 (2000).

579 42. A. D. Weston, R. A. S. Chandraratna, J. Torchia, T. M. Underhill, Requirement for RAR-mediated  
580 gene repression in skeletal progenitor differentiation. *J Cell Biol* **158**, 39–51 (2002).

581 43. M. C. Harrisingh, E. Perez-Nadales, D. B. Parkinson, D. S. Malcolm, A. W. Mudge, A. C. Lloyd, The  
582 Ras/Raf/ERK signalling pathway drives Schwann cell dedifferentiation. *EMBO J* **23**, 3061–3071 (2004).

583 44. I. Napoli, L. A. Noon, S. Ribeiro, A. P. Kerai, S. Parrinello, L. H. Rosenberg, M. J. Collins, M. C.  
584 Harrisingh, I. J. White, A. Woodhoo, A. C. Lloyd, A central role for the ERK-signaling pathway in  
585 controlling Schwann cell plasticity and peripheral nerve regeneration in vivo. *Neuron* **73**, 729–742  
586 (2012).

587 45. I. Cervellini, J. Galino, N. Zhu, S. Allen, C. Birchmeier, D. L. Bennett, Sustained MAPK/ERK  
588 Activation in Adult Schwann Cells Impairs Nerve Repair. *J Neurosci* **38**, 679–690 (2018).

589 46. A. P. W. Johnston, S. Naska, K. Jones, H. Jinno, D. R. Kaplan, F. D. Miller, Sox2-mediated regulation  
590 of adult neural crest precursors and skin repair. *Stem Cell Reports* **1**, 38–45 (2013).

591 47. A. Badache, N. Muja, G. H. De Vries, Expression of Kit in neurofibromin-deficient human Schwann  
592 cells: role in Schwann cell hyperplasia associated with type 1 neurofibromatosis. *Oncogene* **17**, 795–  
593 800 (1998).

594 48. G. A. Mashour, N. Ratner, G. A. Khan, H. L. Wang, R. L. Martuza, A. Kurtz, The angiogenic factor  
595 midkine is aberrantly expressed in NF1-deficient Schwann cells and is a mitogen for neurofibroma-  
596 derived cells. *Oncogene* **20**, 97–105 (2001).

597 49. D. M. Patmore, S. Welch, P. C. Fulkerson, J. Wu, K. Choi, D. Eaves, J. J. Kordich, M. H. Collins, T.  
598 P. Cripe, N. Ratner, *In Vivo* Regulation of TGF- $\beta$  by R-Ras2 Revealed through Loss of the RasGAP  
599 Protein NF1. *Cancer Research* **72**, 5317–5327 (2012).

600 50. J. El-Hoss, T. Cheng, E. C. Carpenter, K. Sullivan, N. Deo, K. Mikulec, D. G. Little, A. Schindeler, A  
601 Combination of rhBMP-2 (Recombinant Human Bone Morphogenetic Protein-2) and MEK (MAP  
602 Kinase/ERK Kinase) Inhibitor PD0325901 Increases Bone Formation in a Murine Model of  
603 Neurofibromatosis Type I Pseudarthrosis. *The Journal of Bone and Joint Surgery* **96**, e117 (2014).

604 51. A. Julien, A. Kanagalingam, E. Martínez-Sarrà, J. Megret, M. Luka, M. Ménager, F. Relaix, C. Colnot,  
605 Direct contribution of skeletal muscle mesenchymal progenitors to bone repair. *Nature Communications*  
606 **12**, 2860 (2021).

607 52. A. C. Masquelet, F. Fitoussi, T. Begue, G. P. Muller, [Reconstruction of the long bones by the  
608 induced membrane and spongy autograft]. *Ann Chir Plast Esthet* **45**, 346–353 (2000).

609 53. M. Logan, J. F. Martin, A. Nagy, C. Lobe, E. N. Olson, C. J. Tabin, Expression of Cre recombinase  
610 in the developing mouse limb bud driven by aPrxl enhancer. *genesis* **33**, 77–80 (2002).

611 54. M. D. Muzumdar, B. Tasic, K. Miyamichi, L. Li, L. Luo, A global double-fluorescent Cre reporter  
612 mouse. *Genesis* **45**, 593–605 (2007).

613 55. L. Madisen, T. A. Zwingman, S. M. Sunkin, S. W. Oh, H. A. Zariwala, H. Gu, L. L. Ng, R. D. Palmiter,  
614 M. J. Hawrylycz, A. R. Jones, E. S. Lein, H. Zeng, A robust and high-throughput Cre reporting and  
615 characterization system for the whole mouse brain. *Nat Neurosci* **13**, 133–140 (2010).

616 56. Y. Zhu, M. I. Romero, P. Ghosh, Z. Ye, P. Charnay, E. J. Rushing, J. D. Marth, L. F. Parada, Ablation  
617 of NF1 function in neurons induces abnormal development of cerebral cortex and reactive gliosis in the  
618 brain. *Genes Dev* **15**, 859–876 (2001).

619



620 **Acknowledgements**

621 We thank A. Henry, A. Guigan and O. Pellé from the Flow Cytometry platforms of IMRB and Imagine  
622 Institute, L. Slimani and K. Henri from Life Imaging Facility of Paris Cité University (Plateforme Imagerie  
623 du Vivant “Micro-CT platform”), all the staff from the Imagine genomic core facility at Imagine Institute  
624 and N. Cagnard from Bioinformatics Platform at Imagine Institute for advice and technical assistance.  
625 We thank A. Julien, C. Goachet, M. Ethel, S. Berger, E. Tacu, E. Paniel, A. Heisler, and M. Mansour for  
626 technical assistance or advice.

627

628 **Fundings**

629 This work was supported by  
630 Association Neurofibromatoses et Recklinghausen (C.C and B.P.), Osteosynthesis and Trauma Care  
631 Foundation (C.C. and St.P.), Agence Nationale de la Recherche-18-CE14-0033 and 21-CE18-007-01  
632 (C.C, P.T. and B.P.), US Department of the Army NF220019 (C.C.), National Institutes of Health NIAMS  
633 R01 AR081671 (C.C. and Ralph Marcucio), and IMRB Cross team award (C.C. and P.T.). S. Perrin and  
634 O. Duchamp de Lageneste were supported by a PhD fellowship from Paris Cité University.

635

636 **Author contributions**

637 Si.P., C.C., P.T. and B.P. conceptualized and formulated the project. Si.P., Sa.P., I.L., V.B, O.D.d.L,  
638 N.P., O.R., M.L., F.C., C.M., T.M., and M.Z. performed experiments. St.P., P.W., S.H-R., K.R., P.T. and  
639 M.M. provided resources. Si.P. performed bioinformatic analyses. C.C. supervised the work. Si.P.  
640 generated the figures. Si.P. and C.C. wrote the original draft of the manuscript. P.T. and B.P reviewed  
641 and edited the manuscript.  
642  
643

644 **Competing interests**

645 The authors declare that they have no competing interests.

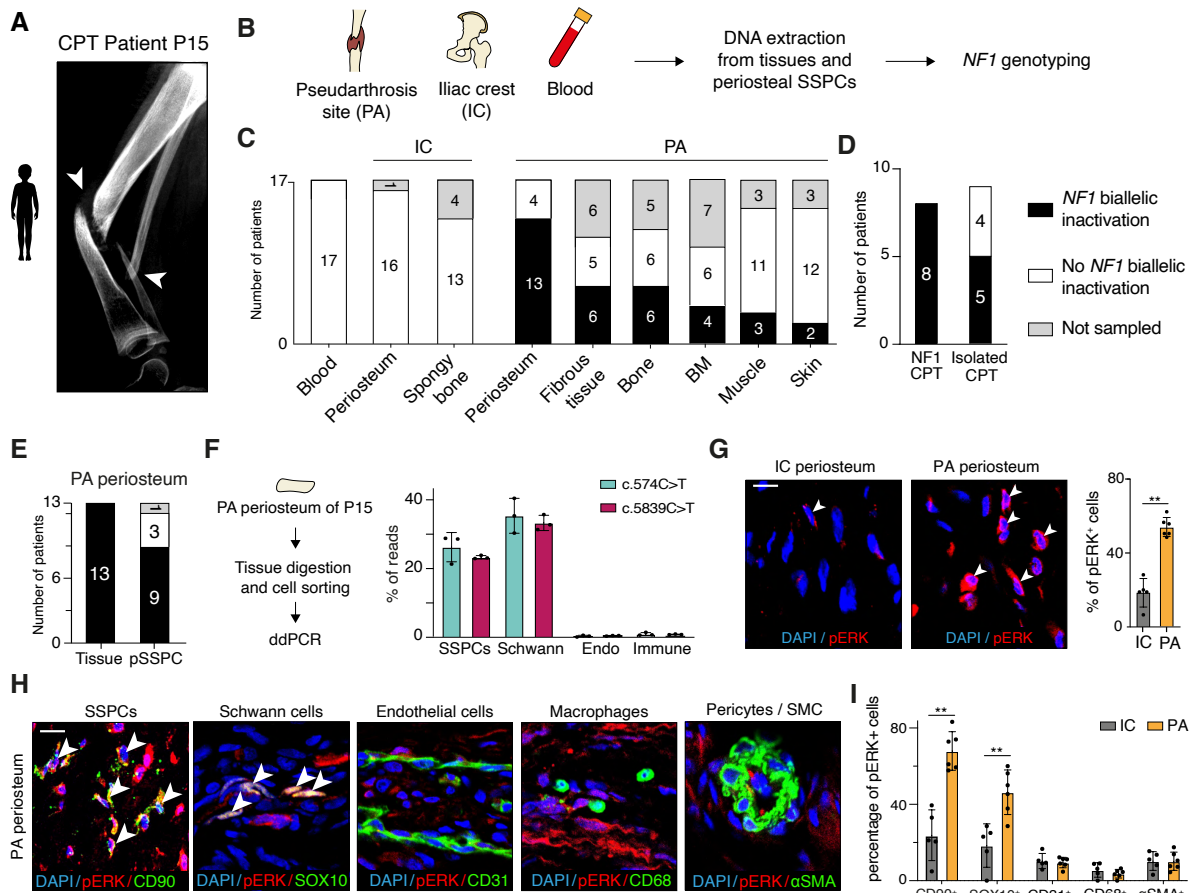
646

647 **Data and materials availability**

648 All data from this study are present in the paper or supplementary materials. Single-nuclei RNAseq  
649 and bulk RNAseq datasets generated for this study are deposited in GEO (GSE232516, GSE232517,  
650 GSE234071) and are publicly available.

651 **Figures**

**Figure 1**



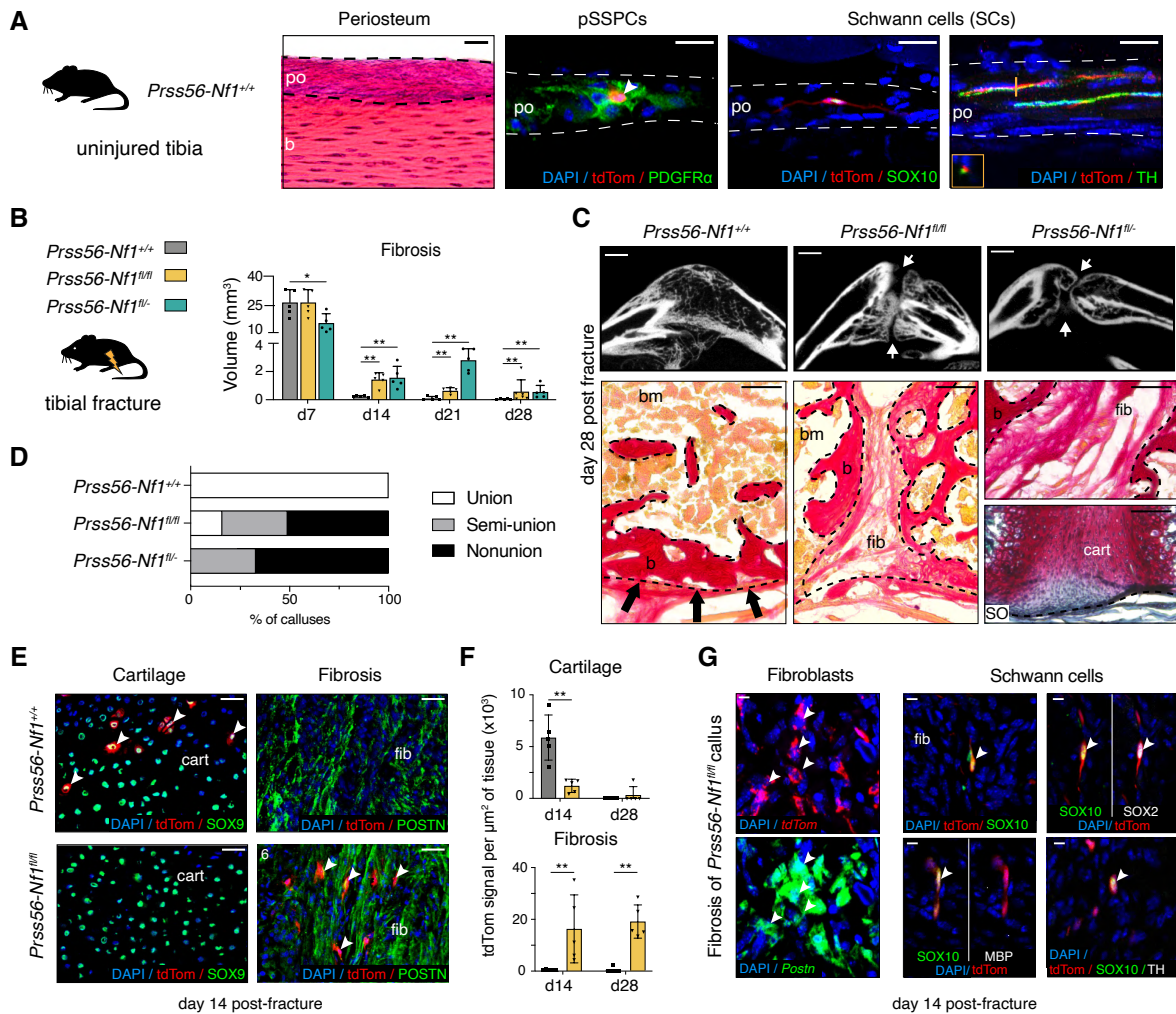
652

653 **Figure 1: Schwann cells and SSPCs within periosteum harbor *NF1* biallelic inactivation in CPT**

654 **A.** X-ray of the tibia and fibula pseudarthrosis (white arrows) of patient with CPT P15. **B.** Experimental  
 655 design. DNA was extracted from tissues or periosteal SSPCs (pSSPCs) collected at the pseudarthrosis  
 656 (PA) site and the iliac crest (IC), and from blood of patients with CPT undergoing surgery, and *NF1*  
 657 targeted sequencing was performed. **C.** *NF1* genotyping of tissues from 17 patients with CPT shows the  
 658 absence of *NF1* biallelic inactivation in blood and IC and the presence of *NF1* biallelic inactivation in the  
 659 periosteum at PA site in 13/17 patients. *NF1* biallelic inactivation was also detected in 6/17 patients in  
 660 fibrous tissue and bone, in 4/17 in bone marrow, in 3/17 in muscle, and in 2/17 in PA site skin. **D.** Number  
 661 of patients with *NF1*-related CPT and isolated CPT carrying *NF1* biallelic inactivation. **E.** *NF1* genotyping  
 662 of periosteum and SSPCs from PA site shows the presence of *NF1* biallelic inactivation in 9/13 patients.  
 663 **F.** Left: experimental design. Cell populations were digested and sorted from PA periosteum of patient

664 P15 and the frequency of the 2 *NF1* point mutations (c.574C>T and c.5839C>T) was determined using  
665 droplet digital PCR (ddPCR). Right: Percentage of the 2 mutations in the different cell populations  
666 showing that Schwann cells and SSPCs carry both *NF1* hits, but not endothelial and immune cells. (n=  
667 3 replicates). **G.** Phospho-ERK (pERK) immunofluorescence on periosteum sections showing number  
668 of pERK+ cells in the periosteum from PA site compared to the periosteum from IC (white arrows).  
669 Quantification of the percentage of pERK+ cells in the periosteum from PA and IC (n=5-6 patients per  
670 group). **H.** Co-immunofluorescence of pERK and CD90, SOX10, CD31, CD68 and  $\alpha$ SMA on PA  
671 periosteum sections. **I.** Quantification of pERK+ cells in PA periosteum compared to IC periosteum (n=  
672 5-6 patients per group). \*\*  $p < 0.01$ . BM: Bone marrow. Endo: endothelial cells. Scale bars: 50 $\mu$ m.  
673

**Figure 2**



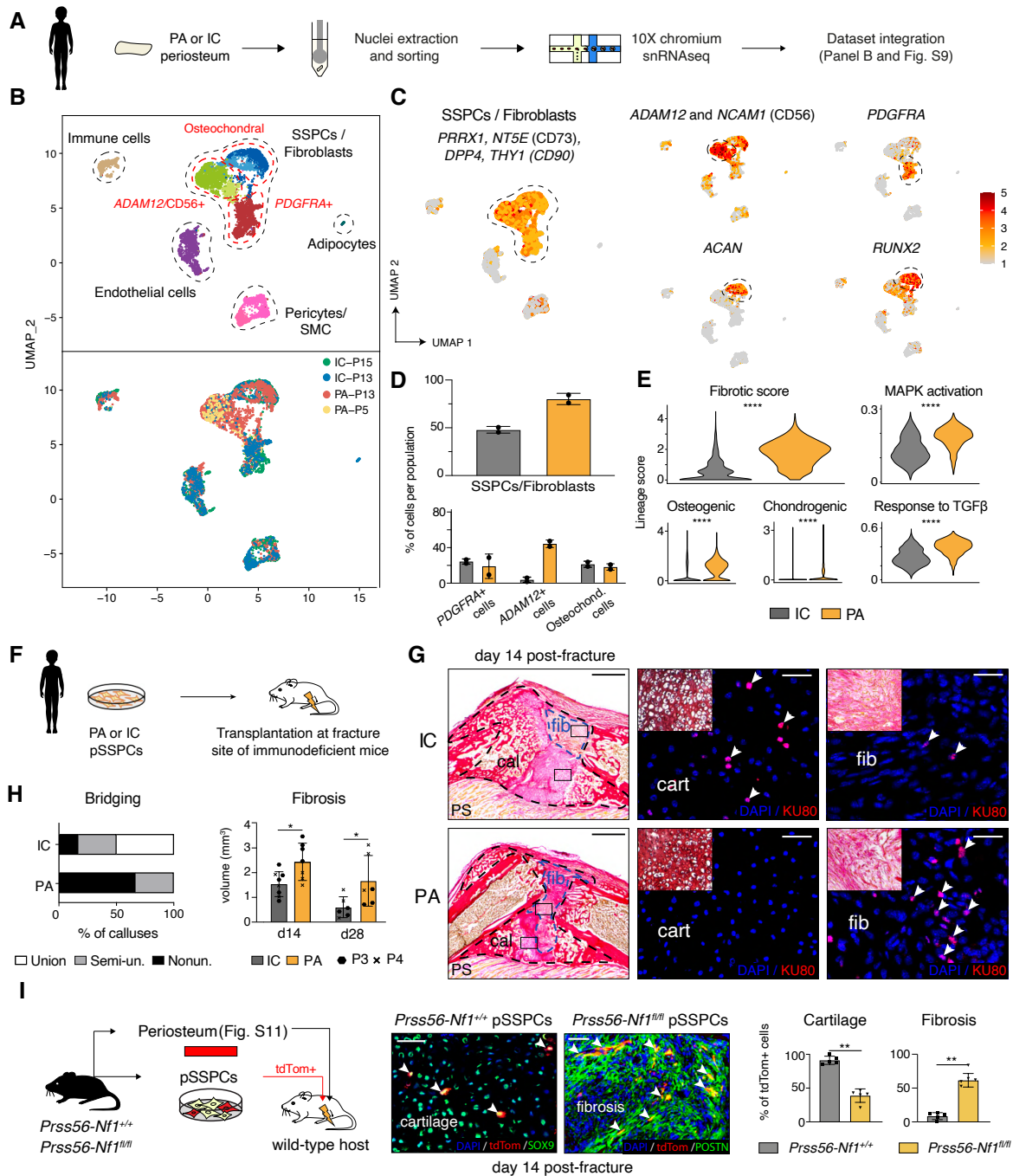
674

675 **Figure 2: Tibial pseudarthrosis in mice lacking *Nf1* gene in boundary cap-derived pSSPCs and**  
 676 **Schwann cells**

677 **A.** Longitudinal sections of uninjured tibia periosteum (po) from 3-month-old *Prss56-Nf1<sup>+/+</sup>* mice stained  
 678 with Hematoxylin-Eosin and immunofluorescence on adjacent sections showing tdTom+ periosteal  
 679 skeletal stem/progenitor cells (pSSPCs) expressing PDGFR $\alpha$  and tdTom+ Schwann cells (SCs)  
 680 expressing SOX10 along TH+ nerves (orange box: transverse imaging). **B.** Left: Experimental design of  
 681 tibial fracture in *Prss56<sup>Cre</sup>; R26<sup>tdTom</sup>; Nf1<sup>+/+</sup>* (*Prss56-Nf1<sup>+/+</sup>*) control, *Prss56<sup>Cre</sup>; R26<sup>tdTom</sup>; Nf1<sup>fl/fl</sup>* (*Prss56-*  
 682 *Nf1<sup>fl/fl</sup>*) and *Prss56<sup>Cre</sup>; R26<sup>tdTom</sup>; Nf1<sup>fl/-</sup>* (*Prss56-Nf1<sup>fl/-</sup>*) mutant mice. Right: Histomorphometric  
 683 quantification of the volume of callus fibrosis at days 7, 14, 21 and 28 post-fracture in *Prss56-Nf1<sup>+/+</sup>*,  
 684 *Prss56-Nf1<sup>fl/fl</sup>* and *Prss56-Nf1<sup>fl/-</sup>* mice (n=5-6 mice per group). **C.** Top: Representative microCT images  
 685 of callus from *Prss56-Nf1<sup>+/+</sup>*, *Prss56-Nf1<sup>fl/fl</sup>* and *Prss56-Nf1<sup>fl/-</sup>* mice at 28 days post-fracture, showing

686 absence of bone bridging in *Prss56-Nf1<sup>fl/fl</sup>* and *Prss56-Nf1<sup>fl/-</sup>* mutant mice (white arrows). Bottom, high  
687 magnification of callus periphery showing bone bridging (black arrows) in *Prss56-Nf1<sup>+/+</sup>* control mice,  
688 and fibrosis and unresorbed cartilage (red, Safranin'O (SO)) in *Prss56-Nf1<sup>fl/fl</sup>* and *Prss56-Nf1<sup>fl/-</sup>* mutant  
689 mice. **D.** Percentage of calluses from *Prss56-Nf1<sup>+/+</sup>*, *Prss56-Nf1<sup>fl/fl</sup>* and *Prss56-Nf1<sup>fl/-</sup>* mice showing bone  
690 union (white), semi-union (grey), or nonunion (black) on microCT scan at day 28 post-fracture (n=6 mice  
691 per group). Bone union was significantly different between mutant and control mice (\*\*\*, p=0.0067) but  
692 not between the mutant groups (p=0.52). **E.** Lineage tracing of Prss56-expressing Boundary Cap (BC)-  
693 derived tdTom+ cells (white arrowheads) in callus cartilage (labelled by SOX9) and fibrosis (labelled by  
694 POSTN) of *Prss56-Nf1<sup>+/+</sup>* and *Prss56-Nf1<sup>fl/fl</sup>* mice 14 days after tibial fracture. **F.** Quantification of tdTom+  
695 signal in cartilage and fibrosis of *Prss56-Nf1<sup>+/+</sup>* and *Prss56-Nf1<sup>fl/fl</sup>* mice 14- and 28-days post-fracture  
696 (n=5 mice per group). **G.** RNAscope and immunofluorescence on callus sections of *Prss56-Nf1<sup>fl/fl</sup>* mice  
697 day 14 post-fracture show the presence of *Postn*-expressing tdTom+ fibroblasts and SOX10+tdTom+  
698 SCs in fibrotic tissue. po: periosteum, b: bone, fib: fibrosis, cart: cartilage, bm: bone marrow, SO:  
699 Safranin'O. p-value: \* p < 0.05, \*\* p < 0.01. Scale bars: Panel A: 25µm. Panel C-microCT: 1mm. Panel  
700 E/C-histology: 100µm. Panel G: 10µm.  
701

**Figure 3**



702

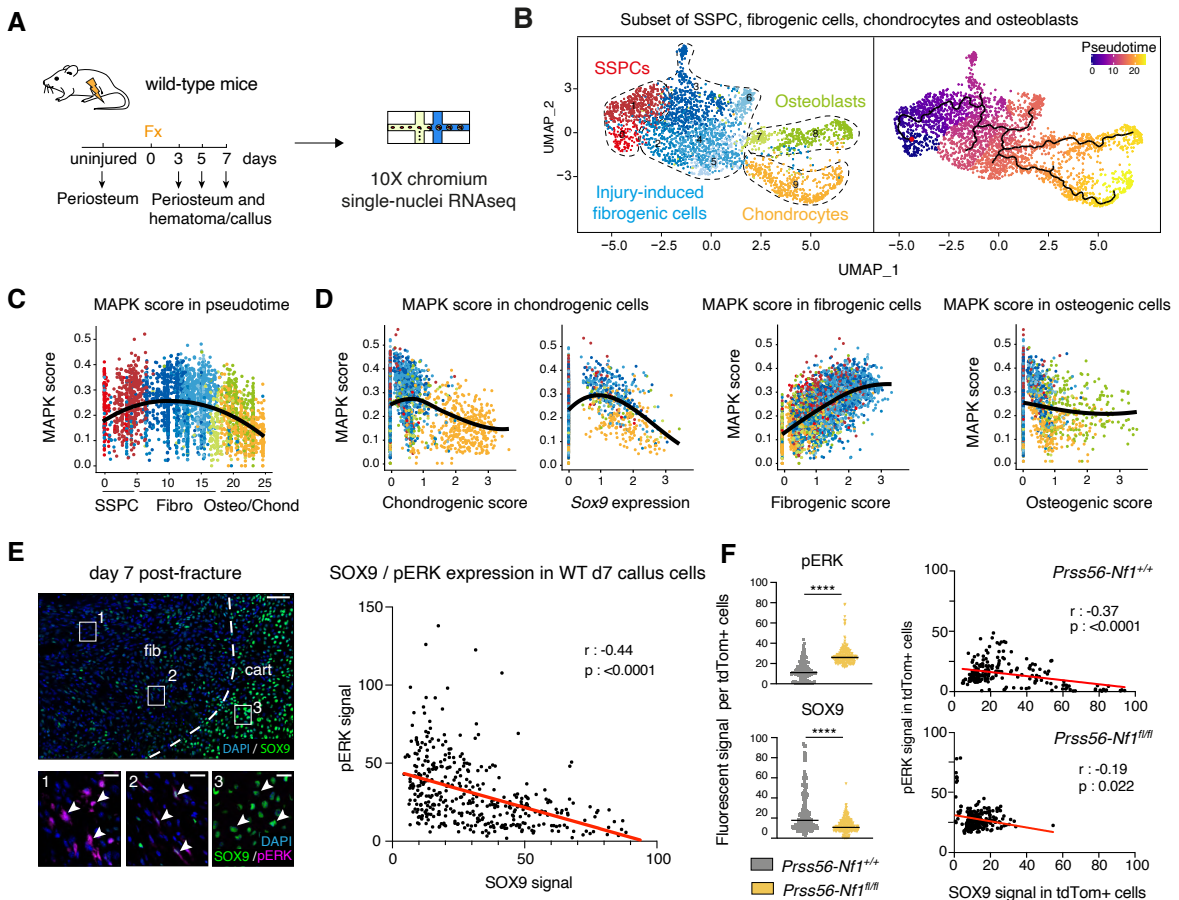
703 **Figure 3: Fibrotic fate of *NF1*-deficient periosteal SSPCs in patients with CPT and *Prss56-Nf1***  
 704 ***KO* mice**

705 **A.** Experimental design. Nuclei were extracted from PA or IC periosteum, sorted, and processed for  
 706 single-nuclei RNAseq. The datasets were integrated for analyses. **B.** UMAP projection of color-coded  
 707 clustering (top) and sampling (bottom) of the integration of the datasets of IC periosteum from P15 (IC-

708 P15, green), IC periosteum from P13 (IC-P13, blue), PA periosteum from P13 (PA-P13, red) and PA  
709 periosteum from P5 (PA-P5, yellow). **C.** Feature plots of the SSPC/fibroblast lineage score and  
710 *ADAM12/NCAM1* (Neural Cell Adhesion Molecule 1), *PDGFRA*, *ACAN*, and *RUNX2* gene expression.  
711 **D.** Percentage of cells from PA and IC samples in SSPC/fibroblast populations and in *ADAM12+*,  
712 *PDGFRA+*, and osteochondral clusters. **E.** Violin plots of the fibrotic, osteogenic, chondrogenic, MAPK  
713 activation, and cellular response to TGF $\beta$  lineage score in IC and PA. **F.** Experimental design. PA or IC  
714 pSSPCs from patients P3 and P4 were transplanted at the fracture site of immunodeficient mice. **G.**  
715 Representative callus sections stained with Picrosirius (PS). High magnification of cartilage stained with  
716 Safranin'O and fibrosis stained with PS and immunofluorescence of the human KU80 protein at day 14  
717 post-fracture showing that IC pSSPC-derived cells are located mostly in cartilage while PA pSSPC-  
718 derived cells are located in fibrosis (white arrow). **H.** Left: Percentage of callus grafted with PA or IC  
719 pSSPCs showing union, semi-union, and nonunion at day 28 post-fracture. Right: Volume of fibrosis in  
720 day 14 and 28 post-fracture callus of immunodeficient mice grafted with human pSSPCs from IC and  
721 PA (n=6-8 mice per group). **I.** Left: Experimental design. Periosteum or cultured tdTom<sup>+</sup> periosteal  
722 skeletal stem/progenitor cells (pSSPCs) were isolated from *Prss56-Nf1<sup>+/+</sup>* or *Prss56-Nf1<sup>fl/fl</sup>* mice and  
723 transplanted at the fracture site of wild-type hosts. Middle: Representative images of the contribution of  
724 grafted tdTom<sup>+</sup> cells (white arrows) showing cells from *Prss56-Nf1<sup>+/+</sup>* mice detected in cartilage (labelled  
725 by SOX9) and cells from *Prss56-Nf1<sup>fl/fl</sup>* mice detected in fibrosis (labelled by POSTN). Right: Percentage  
726 of grafted tdTom<sup>+</sup> cells in cartilage and fibrosis (n=5 mice per group). SMC: smooth muscle cells, cal:  
727 callus, fib: fibrosis, cart: cartilage. p-value: \* p < 0.05, \*\* p < 0.01, \*\*\*\* p < 0.0001. Scale bars: Panel G:  
728 Low magnification: 1mm. High magnification: 100 $\mu$ m. Panel I: 100 $\mu$ m.



**Figure 4**



729

730 **Figure 4: Overactivation of MAPK pathway causes fibrotic differentiation of *Nf1*-deficient**  
 731 **pSSPCs**

732 **A.** Experimental design of single nuclei RNAseq (snRNAseq) experiment. Nuclei were isolated from  
 733 uninjured periosteum, or periosteum and hematoma of wild type mice at days 3, 5, and 7 post- tibial  
 734 fracture, sorted, and processed for snRNAseq. **B.** UMAP projection of clustering and monocle  
 735 pseudotime trajectory of the subset of SSPCs, injury-induced fibrogenic cells, osteoblasts, and  
 736 chondrocytes from integrated uninjured, day 3, day 5, and day 7 post-fracture samples. The four  
 737 populations are delimited by black dashed lines. **C.** Scatter plot of MAPK score along pseudotime. **D.**  
 738 Scatter plots of MAPK score along chondrogenic lineage score, *Sox9* expression, fibrogenic, and  
 739 osteogenic lineage scores. **E.** Immunofluorescence of SOX9 and phospho-ERK (pERK) in day 7 post-  
 740 fracture callus section of wild type (WT) mice. Quantification and correlation of SOX9 and pERK signal  
 741 per cell (red line) (n = 397 cells from 8 callus sections of 4 mice). Scale bars: low magnification, 150µm;



742 high magnification, 25 $\mu$ m. **F.** Left: Quantification of SOX9 and pERK fluorescent signal per tdTom+ cells  
743 in day 7 post-fracture callus of *Prss56-Nf1<sup>+/+</sup>* and *Prss56-Nf1<sup>fl/fl</sup>* mice. Right: Correlation analysis of pERK  
744 and SOX9 signals in tdTom+ cells in *Prss56-Nf1<sup>+/+</sup>* (top) and *Prss56-Nf1<sup>fl/fl</sup>* (bottom) mice (n = 209 to  
745 238 cells from 9 sections of 3 mice per group). cart: cartilage, fib: fibrosis. \*\*\*\*: p < 0.0001.

746

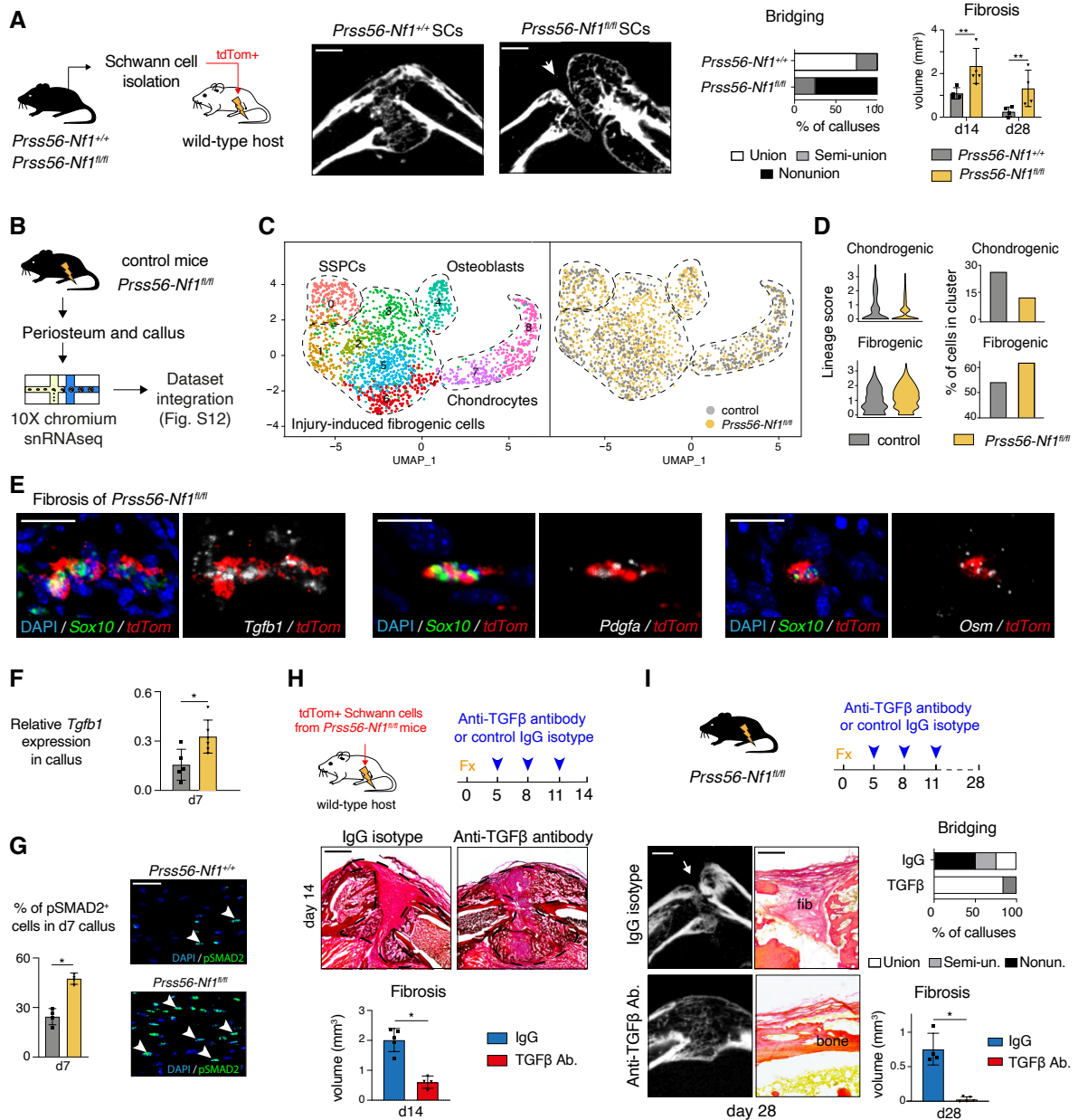
747

748

749

750

**Figure 5**



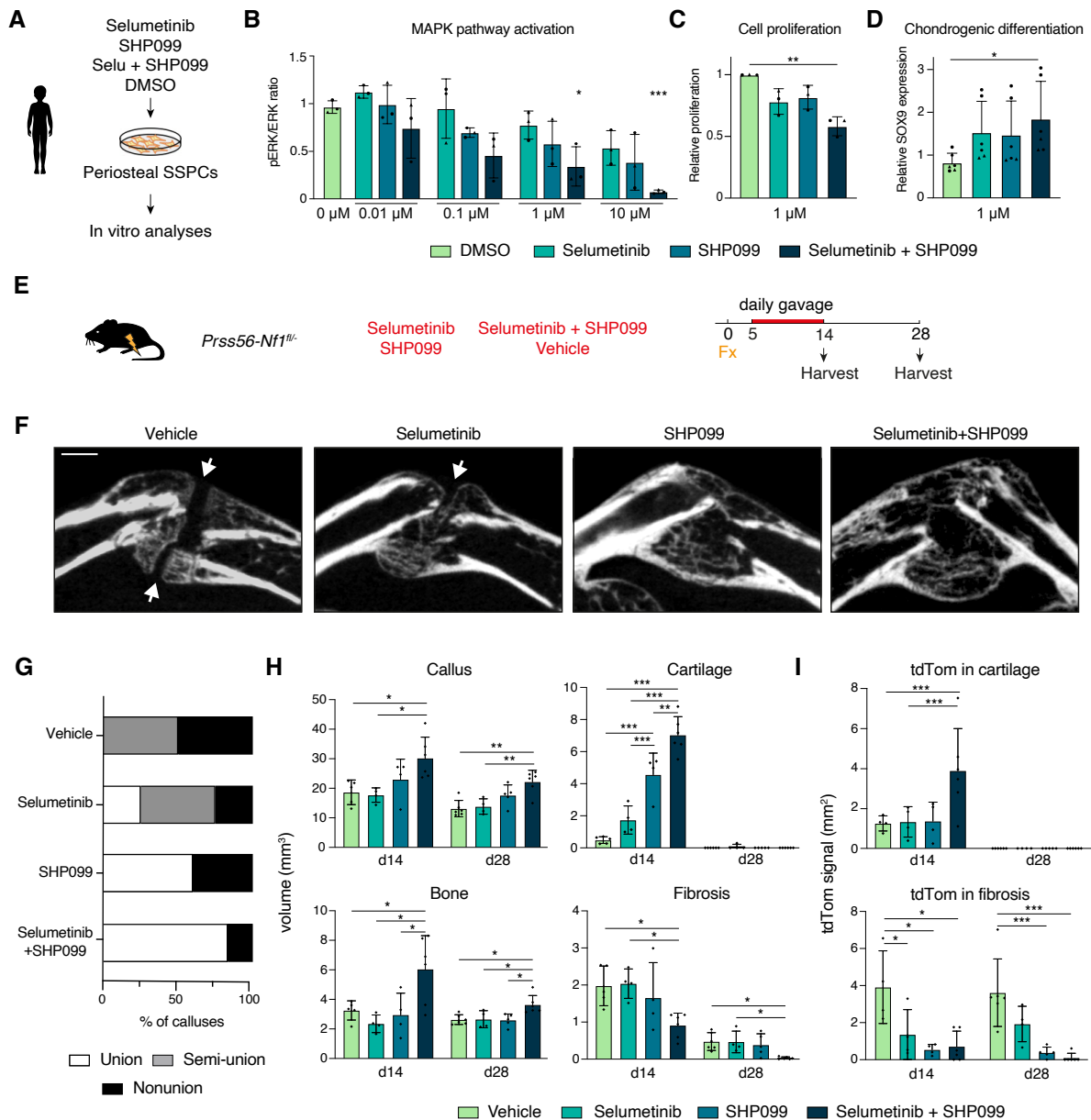
751

752 **Figure 5: Pro-fibrotic effect of *Nf1*-deficient Schwann cells in fibrous nonunion**

753 **A.** Left: Experimental design. tdTom+ Schwann cells (SCs) were isolated from *Prss56-Nf1<sup>+/+</sup>* or *Prss56-*  
 754 *Nf1<sup>fl/fl</sup>* mice and transplanted at the fracture site of wild-type hosts. Middle: MicroCT images of 28 days  
 755 post-fracture calluses of wild-type mice grafted with SCs from *Prss56-Nf1<sup>+/+</sup>* or *Prss56-Nf1<sup>fl/fl</sup>* mice,  
 756 showing absence of bridging in mice grafted with *Nf1*-deficient SCs (white arrow). Right: Percentage of  
 757 day 28 post-fracture calluses showing union, semi-union, or nonunion. Volume of callus fibrosis at 14  
 758 and 28 days post-fracture (n=4-5 mice per group). **B.** Experimental design. Nuclei were isolated from  
 759 periosteum and hematoma at day 7 post-fracture of control or *Prss56-Nf1<sup>fl/fl</sup>* mice and processed for

760 snRNAseq. Datasets were integrated. **C.** UMAP projection of SSPC, injury-induced fibrogenic,  
761 chondrogenic, and osteogenic cell subsets from the integrated day 7 post-fracture control and *Prss56-*  
762 *Nf1<sup>fl/fl</sup>* datasets. **D.** Violon plot of chondrogenic and fibrogenic lineage scores per dataset. Percentage of  
763 cells per cluster. **E.** RNAscope experiment on day 7 post-fracture callus from *Prss56-Nf1<sup>fl/fl</sup>* mice shows  
764 the expression of *Tgfb1*, *Pdgfa*, and *Osm* by *Sox10*-, *tdTom*-expressing Schwann cells in callus fibrosis.  
765 **F.** Relative expression of *Tgfb1* in day 7 post-fracture callus of *Prss56-Nf1<sup>+/+</sup>* or *Prss56-Nf1<sup>fl/fl</sup>* mice (n=5  
766 mice per group). **G.** Percentage of phospho-SMAD2 positive (pSMAD2+) cells in the day 7 post-fracture  
767 callus of *Prss56-Nf1<sup>+/+</sup>* or *Prss56-Nf1<sup>fl/fl</sup>* mice (n=4 mice per group). Representative pSMAD2  
768 immunofluorescence of *Prss56-Nf1<sup>+/+</sup>* or *Prss56-Nf1<sup>fl/fl</sup>* callus. **H.** Top: Experimental design. Wild-type  
769 mice grafted with tdTom+ Schwann cells from *Prss56-Nf1<sup>fl/fl</sup>* mice were treated with blocking TGFβ  
770 antibody or IgG1 control isotype at days 5, 8, and 11 post-fracture. Middle: Picrosirius staining of fracture  
771 calluses at 14 days post-fracture. Bottom: Volume of callus fibrosis (n=4-5 mice per group). **I.** Top:  
772 Experimental design. *Prss56-Nf1<sup>fl/fl</sup>* mice were treated with blocking TGFβ antibody or IgG1 control  
773 isotype at days 5, 8, and 11 post-fracture. Middle: MicroCT images of callus of *Prss56-Nf1<sup>fl/fl</sup>* mice treated  
774 with IgG1 isotype control or TGFβ blocking antibody at 28 days post-fracture. High magnification of the  
775 callus periphery stained with Picrosirius. Bottom left: percentage of day 28 post-fracture calluses  
776 showing union (white), semi-union (grey) or nonunion (black) on microCT scan. Bottom right: Volume of  
777 callus fibrosis of *Prss56-Nf1<sup>fl/fl</sup>* mice treated with blocking TGFβ antibody or IgG1 isotype control at 28  
778 days post-fracture. (n=4-5 mice per group). p-value: \* p < 0.05, \*\* p < 0.01. Scale bars: Panel A/H 1mm.  
779 Panel E: 10μm. Panel G 50μm, panel I: Low magnification: 1mm, High magnification: 250 μm.

**Figure 6**



780

781 **Figure 6: Combined MEK and SHP2 inhibition prevents fibrous nonunion in *Prss56-Nf1* KO mice**

782 **A.** Experimental design. Periosteal SSCs from PA site of patients with CPT were treated with MEK

783 inhibitor (selumetinib), SHP2 inhibitor (SHP099), MEK and SHP2 inhibitors (selumetinib and SHP099),

784 or vehicle (DMSO) for in vitro analyses. **B.** MAPK pathway activation in pSSPCs from PA site treated

785 with selumetinib, SHP099, selumetinib and SHP099, or DMSO measured by the pERK/ERK ratio on

786 Western blot. Statistical significance was determined compared to DMSO control (n=3 patients). **C.**

787 Reduced in vitro proliferation of pSSPCs from PA site treated with combined selumetinib and SHP099

788 (n=3 patients). **D.** Increased in vitro chondrogenic differentiation measured by SOX9 expression of  
789 pSSPCs from PA site treated with combined selumetinib and SHP099 (n=3 patients in duplicates). **E.**  
790 Experimental design. *Prss56-Nf1<sup>fl/-</sup>* mice were treated by oral gavage with selumetinib, SHP099,  
791 selumetinib and SHP099, or vehicle from days 5 to 14 post-fracture. **F.** Representative microCT images  
792 of callus from *Prss56-Nf1<sup>fl/-</sup>* mice at 28 days post-fracture, with bone bridging indicated by white arrows.  
793 **G.** Percentage of calluses from treated and control *Prss56-Nf1<sup>fl/-</sup>* mice showing bone union (white), semi-  
794 union (grey), or nonunion (black) on microCT scan at day 28 post-fracture (n=4-6 mice per group). **H.**  
795 Volume of callus, cartilage, bone, and fibrosis at days 14 and 28 post-fracture in treated and control  
796 *Prss56-Nf1<sup>fl/-</sup>* mice (n=4-6 mice per group). **I.** Surface of tdTom signal in cartilage and fibrosis of day 14  
797 and 28 callus from treated and control *Prss56-Nf1<sup>fl/-</sup>* mice. Scale bars: 1mm. p-value: \* p < 0.05, \*\* p <  
798 0.01, \*\*\* p < 0.001.  
799